

This is a repository copy of *Effects of microcompartmentation on flux distribution and metabolic pools in Chlamydomonas reinhardtii* chloroplasts.

White Rose Research Online URL for this paper:

<https://eprints.whiterose.ac.uk/id/eprint/137065/>

Version: Accepted Version

Article:

Kuken, A., Sommer, F., Yaneva-Roder, L. et al. (8 more authors) (2018) Effects of microcompartmentation on flux distribution and metabolic pools in *Chlamydomonas reinhardtii* chloroplasts. *eLife*. ISSN: 2050-084X

<https://doi.org/10.7554/eLife.37960>

Reuse

Items deposited in White Rose Research Online are protected by copyright, with all rights reserved unless indicated otherwise. They may be downloaded and/or printed for private study, or other acts as permitted by national copyright laws. The publisher or other rights holders may allow further reproduction and re-use of the full text version. This is indicated by the licence information on the White Rose Research Online record for the item.

Takedown

If you consider content in White Rose Research Online to be in breach of UK law, please notify us by emailing eprints@whiterose.ac.uk including the URL of the record and the reason for the withdrawal request.

Effects of microcompartmentation on flux distribution and metabolic pools in *Chlamydomonas reinhardtii* chloroplasts

Küken, A.^{1,2}, Sommer, F.^{1†}, Yaneva-Roder, L.¹, Mackinder, L.^{3‡}, Höhne, M.¹, Geimer, S.⁴, Jonikas, M.C.^{3§}, Schroda, M.^{1†}, Stitt, M.¹, Nikoloski, Z.^{1,2}, Mettler-Altmann, T.^{1,5*}

¹Max Planck Institute of Molecular Plant Physiology, 14476 Potsdam-Golm, Germany

²Bioinformatics Group, Institute of Biochemistry and Biology, University of Potsdam, Karl-Liebknecht-Str. 24-25, 14476 Potsdam, Germany

³Department of Plant Biology, Carnegie Institution for Science, Stanford, CA 94305, USA

⁴Institute of Cell Biology, University of Bayreuth, 95440 Bayreuth, Germany

⁵Cluster of Excellence on Plant Sciences and Institute of Plant Biochemistry, Heinrich-Heine University, 40225 Düsseldorf, Germany

[†]Current address: Molecular Biotechnology and Systems Biology, University of Kaiserslautern, 67663 Kaiserslautern, Germany

[‡]Current address: Department of Biology, University of York, York, YO10 5DD, UK

[§]Current address: Department of Molecular Biology, Princeton University, Princeton, NJ 08544, USA

*Correspondence to: tabea.mettler@hhu.de

ABSTRACT

Cells and organelles are not homogeneous but include microcompartments that alter the spatiotemporal characteristics of cellular processes. The effects of microcompartmentation on metabolic pathways are however difficult to study experimentally. The pyrenoid is a microcompartment that is essential for a carbon concentrating mechanism (CCM) that improves the photosynthetic performance of eukaryotic algae. Using *Chlamydomonas reinhardtii*, we obtained experimental data on photosynthesis, metabolites, and proteins in CCM-induced and CCM-suppressed cells. We then employed a computational strategy to estimate how fluxes through the Calvin-Benson cycle are compartmented between the pyrenoid and the stroma. Our model predicts that ribulose-1,5-bisphosphate (RuBP), the substrate of Rubisco, and 3-phosphoglycerate (3PGA), its product, diffuse in and out of the

31 pyrenoid, respectively, with higher fluxes in CCM-induced cells. It also indicates that there is
32 no major diffusional barrier to metabolic flux between the pyrenoid and stroma. Our
33 computational approach represents a stepping stone to understanding
34 microcompartmentalized CCM in other organisms.

INTRODUCTION

Compartments of eukaryotic cells are surrounded by a single- or multiple-layer lipid membrane. Both eukaryotic and prokaryotic cells also include microcompartments that are not separated from the rest of the cell by a lipid membrane (for reviews, see Giordano, Beardall, & Raven, 2005; Hyman, Weber, & Juelicher, 2014). In bacteria they are surrounded by protein shells (for reviews, see Kerfeld & Melnicki, 2016; Yeates, Crowley, & Tanaka, 2010). Such microcompartments may partition metabolic pools and enzymes; therefore, they can directly affect the operation of metabolic pathways. Microcompartments may serve diverse roles, from storage of special compounds (Bazylinski & Frankel, 2004), degradation of small molecules (Bobik, Havemann, Busch, Williams, & Aldrich, 1999), facilitation of enzyme clustering (Castellana et al., 2014), to regulating the activity of particular metabolic pathways.

The first described bacterial microcompartment was the carbon-fixing carboxysome in cyanobacteria (Drews & Niklowitz, 1956). It enables the cell to accumulate carbon dioxide (CO₂) in the vicinity of Rubisco, which enhances the carboxylation rate. The carboxysome is an essential part of the cyanobacterial carbon concentrating mechanism (CCM). There are two types of carboxysomes, the alpha and beta carboxysome, and the structure and function of both types have been well-studied (Kerfeld & Melnicki, 2016). Loss of structural proteins results in carboxysome-less mutants that are unable to grow under ambient CO₂ conditions (Berry, Fischer, Kruip, Hauser, & Wildner, 2005; Ogawa, Amichay, & Gurevitz, 1994; Woodger, Badger, & Price, 2005). Two other microcompartmentalized pathways, namely, propanediol and ethanolamine utilization, have also been experimentally explored in bacteria (Chen, Andersson, & Roth, 1994; Stojiljkovic, Baumler, & Heffron, 1995). The role of the propanediol utilization (Pdu) microcompartment in *Salmonella enterica* is the degradation of 1,2-propanediol, a product of anaerobic sugar breakdown, without the release of the

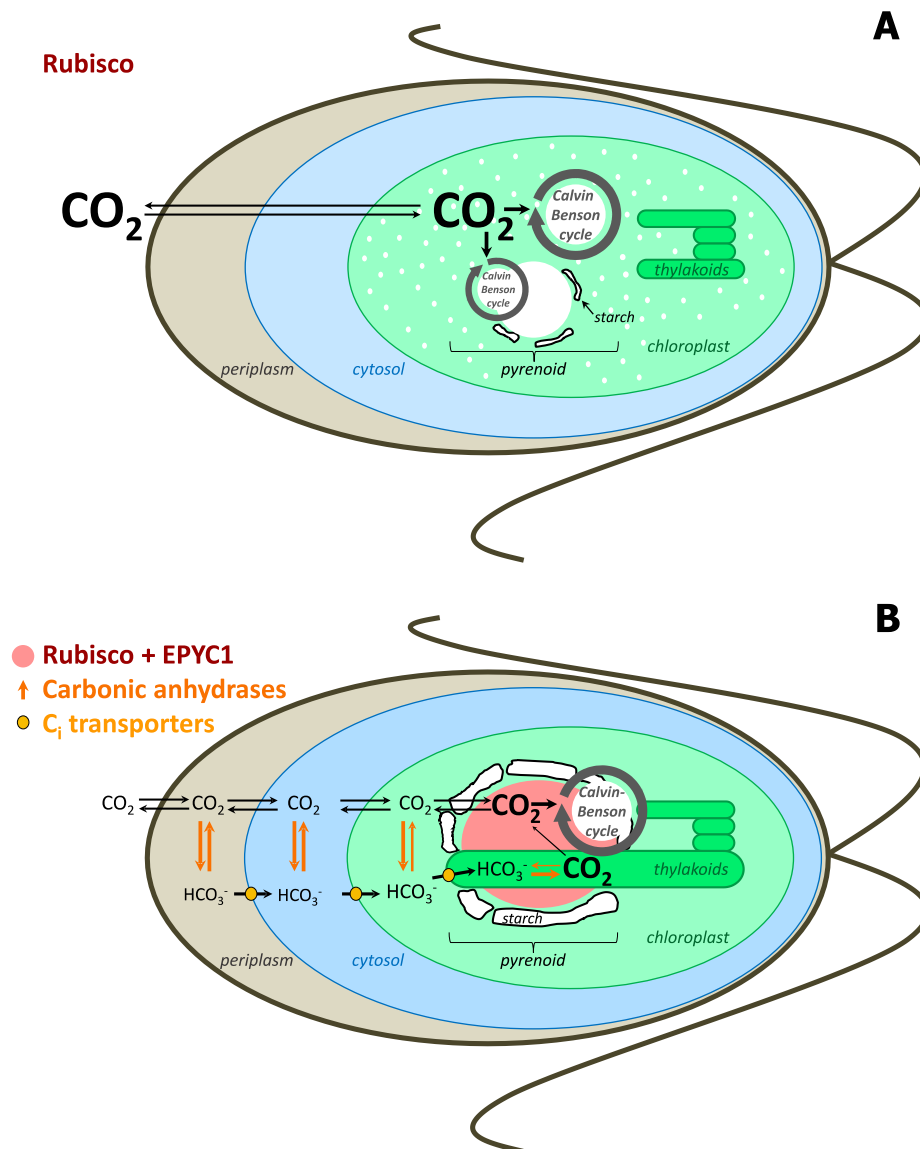
degradation intermediate propionaldehyde. Propionaldehyde is toxic and, once in the cytosol, causes damage to DNA (Sampson & Bobik, 2008). A similar role was suggested for the ethanolamine utilization (Eut) microcompartment in the detoxification of acetaldehyde produced during ethanolamine catabolism (Moore & Escalante-Semerena, 2016). Microcompartments are also known in eukaryotes, including: metabolic compartments in liver (Fujiwara & Itoh, 2014) and muscle cells (Saks, Beraud, & Wallimann, 2008), and the pyrenoid in chloroplasts of green algae (Gibbs, 1962).

Despite these discoveries, it remains challenging to determine the implications of microcompartments for cellular physiology, and to study their function under different conditions that may induce or suppress their formation. This task is experimentally tedious and often not feasible due to challenges in separating the microcompartment (Saks et al., 2008). Here we present a combined experimental and mathematical approach to quantify metabolic exchange fluxes at the boundary of the pyrenoid in the chloroplast of the green alga *Chlamydomonas reinhardtii* under two environmental conditions, atmospheric CO₂ with an active CCM; and high CO₂, where the CCM is inactive.

Different CCMs have evolved in higher plants, algae and cyanobacteria to cope with the relatively low amounts of CO₂ in the atmosphere (currently 0.03-0.04%) and to compensate for the low affinity of Rubisco for CO₂ under these conditions (Delgado, Medrano, Keys, & Parry, 1995; Tcherkez, Farquhar, & Andrews, 2006). As already mentioned, CCM in cyanobacteria requires microcompartments called carboxysomes. In eukaryotic green algae, a microcompartment called the pyrenoid is crucial for the establishment of a CCM (Caspari et al., 2017; Genkov, Meyer, Griffiths, & Spreitzer, 2010) (Figure 1). There is no membrane or protein shell surrounding the pyrenoid which, like many of these non-membrane microcompartments (for review, see Hyman et al., 2014), was recently described as a liquid-

like organelle formed by phase separation from the chloroplast stroma (Rosenzweig et al., 2017).

Pyrenoids are known to contain Rubisco (Kuchitsu, Tsuzuki, & Miyachi, 1988b, 1991; McKay, Gibbs, & Vaughn, 1991), Rubisco activase (McKay et al., 1991) and EPYC1, which has been proposed to be a structural protein in the pyrenoid (Mackinder et al., 2016). Immunolocalisation studies showed that about 40% and 90% of the total Rubisco is located in the pyrenoid under high CO₂ and atmospheric CO₂, respectively, while the rest is distributed in the stroma (Borkhsenius, Mason, & Moroney, 1998). Under ambient CO₂ when CCM is induced, experimental evidence suggests that the inorganic carbon (C_i, the sum of CO₂, CO₃²⁻, HCO₃⁻ and H₂CO₃) is actively transported across the membrane of the cell and accumulated as HCO₃⁻ in the thylakoid lumen (for reviews, see Grossman et al., 2007; Jungnick et al., 2014; Moroney & Ynalvez, 2007; Spalding, 2008; Wang, Stessman, & Spalding, 2015). These luminal regions have highly branched tubules that reach into the pyrenoid and may facilitate movement of bicarbonate, CO₂ and other small molecules (Engel et al., 2015). A carbonic anhydrase (CAH3), essential for the CCM, is localized to the lumen regions that pass through the pyrenoid and is thought to catalyze the dehydration of HCO₃⁻ to CO₂, as the preferred form of C_i at the low pH of the lumen (Duanmu, Wang, & Spalding, 2009; Sinetova, Kupriyanova, Markelova, Allakhverdiev, & Pronina, 2012). The resulting CO₂ may then diffuse back across the lumen membrane where it serves as concentrated substrate for the nearby Rubisco. A starch sheath, of unclear function, surrounds the pyrenoid, but only under ambient CO₂ conditions (Kuchitsu, Tsuzuki, & Miyachi, 1988a; Ramazanov et al., 1994). The starch sheath was suggested to serve as a diffusional barrier for CO₂ and therefore potentially also larger molecules such as metabolites, although the existing experimental evidence is inconsistent with this hypothesis (Badger & Price, 1994; Villarejo, Martinez, Plumed, & Ramazanov, 1996).



109

110 **Figure 1. Simplified scheme of CBC cycle with and without carbon-concentrating mechanism (CCM) in**
 111 ***Chlamydomonas reinhardtii*.** Under high CO₂ conditions, no CCM is established (A). After exposure to
 112 ambient CO₂, a CCM is induced (B). As most of Rubisco and the other CBC enzymes are in the stroma under
 113 high CO₂, most CBC flux is in the stroma (big grey circle in the stroma) and only partly involves the pyrenoid
 114 (smaller grey circle) (A). As most of Rubisco is inside the pyrenoid under ambient CO₂, the CBC requires
 115 movement of selected metabolites between the stroma and pyrenoid (big grey circle) (B). To find out the exact
 116 differences of flux distribution between stroma and pyrenoid under these two conditions and how metabolites
 117 are exchanged between the two microcompartments were the aims of this study. Scheme adapted and simplified
 118 from Borkhsenius et al. (1998), Moroney et al. (2011), Wang, Duanmu, and Spalding (2011), Engel et al.
 119 (2015) and Mackinder et al. (2016).

120

121 What does the location of Rubisco in the pyrenoid mean for the rest of the carbon fixation
 122 pathway? The current model of CCM assumes that, apart from Rubisco, the remaining

enzymes of the Calvin-Benson cycle (CBC) are situated in the stroma (Jungnick et al., 2014). This implies that the substrate and product of the carboxylation reaction catalyzed by Rubisco, ribulose-1,5-bisphosphate (RuBP) and 3-phosphoglycerate (3PGA), need to move in and out of the pyrenoid, respectively. This assumption is supported by immunolocalisation studies that failed to detect glyceraldehyde 3-phosphate dehydrogenase (GAPDH), aldolase (FBA + SBA) catalyzing the two aldol reactions of the CBC that produce fructose-1,6-bisphosphate (FBP) and sedoheptulose-1,7-bisphosphate (SBP), ribose-phosphate isomerase (RPI) or phosphoribulokinase (PRK) in pyrenoids (Kuchitsu et al., 1991; Süß, Prokhorenko, & Adler, 1995). Such methods, however, are not well suited to demonstrate absence, and experimental evidence is still lacking for the localization of the remaining CBC enzymes (phosphoglycerokinase (PGK), triosephosphate isomerase (TPI), transketolase (TRK), fructose-1,6-bisphosphatase (FBPase), sedoheptulose-1,7-bisphosphatase (SBPase), and ribulose-phosphate epimerase (RPE)). Furthermore, the evidence for absence of CBC enzymes from the pyrenoid is not fully consistent as biochemical studies indicate PRK may be in close association with the pyrenoid (Holdsworth, 1971; McKay & Gibbs, 1991). Additionally, Rubisco is differently distributed under ambient and high CO₂ (Borkhsenius et al., 1998) implying that the flux of the CBC that takes place in the pyrenoid may differ between these two conditions.

Our study aims to experimentally localize all CBC enzymes, and to measure Calvin-Benson cycle intermediate levels under high and ambient CO₂. These data are then used in combination with mathematical modeling to estimate fluxes through the CBC in the stroma and the pyrenoid under these two CO₂ conditions. Our approach allows us to determine the exchange of fluxes at the boundary of the pyrenoid and to investigate the mode of transport of the exchanged metabolites.

RESULTS

Distribution of Calvin-Benson cycle enzymes

C. reinhardtii CC1690 cells were grown under low CO₂ (LC), which fully induced the CCM (Figure 2-figure supplement 1). In addition, we obtained data from cells grown under high CO₂ (HC), where the induction of a CCM was suppressed.

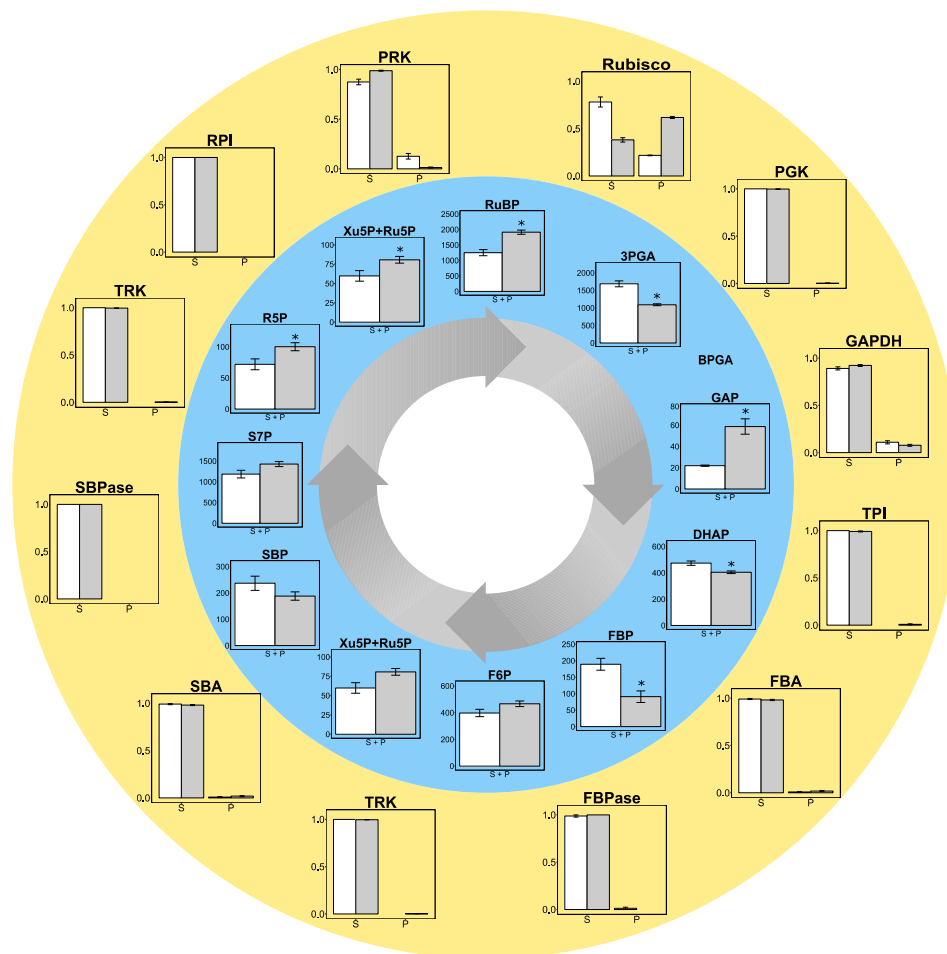


Figure 2. Experimental data for protein distributions (outer yellow circle) and metabolite concentrations (inner blue circle) in CCM-suppressed (white bars, HC) and CCM-induced (grey bars, LC for proteins and LC* for metabolites) conditions. *Chlamydomonas reinhardtii* CC1690 cells were grown under high CO₂ (HC for proteins and metabolites; white bars), ambient CO₂ (LC for proteins; grey bars) and ambient CO₂ bubbled for 15 min with high CO₂ (LC* for metabolites; grey bars). Enzyme distribution between a pyrenoid-enriched fraction (P) and a stroma-enriched fraction (S) was determined by enzyme activity measurements (Rubisco; n = 4 ± SE) and shotgun proteomics (all other proteins; n = 4 ± SE). Metabolites of the Calvin-Benson cycle (CBC) in total cells were measured by HPLC-MS/MS. The metabolite concentrations were normalized to the chloroplast volume as described in the text and Supplementary file 1D, and given as absolute concentrations

(μM) in the chloroplast, which includes both microcompartments, the stroma and the pyrenoid (S + P) ($n = 4 \pm \text{SE}$). Student's t -test ($\alpha = 0.05$), significantly changed metabolites are marked with one asterisk.

C. reinhardtii was fractionated to provide samples enriched for stroma proteins and for pyrenoid-associated proteins according to Mackinder et al. (2016), followed by quantification of the abundance of enzymes involved in the CBC and starch synthesis, using either an enzymatic assay or shotgun proteomics (Figure 2, Supplementary file 1A + B). More than 61.8% of the Rubisco was found in the pyrenoid in LC grown cells, and about 21.8% in HC grown cells. Apart from GAPDH (8% in LC and 11% in HC grown cells) and PRK (13% in HC grown cells but $< 2\%$ in LC grown cells) less than 2% of the other CBC proteins was detected in the pyrenoid-enriched fractions. The $< 2\%$ of CBC proteins found in the pyrenoid-enriched fractions may represent experimental error, and resembled the distribution of PGM and AGPase (0.6 - 1.9% in the pyrenoid).

The localization of most of the CBC enzymes was further confirmed by confocal microscopy of proteins tagged with the yellow fluorescence protein Venus of cells grown under ambient CO_2 (Nagai et al., 2002) (Figure 3, Supplementary file 2). This was of particular interest as different isoforms exist for some of the CBC proteins (Rubisco small subunit, GAPDH, FBPase and aldolase). The proteins encoded by the two Rubisco small subunit genes (*RBCS1* and *RBCS2*) both showed strong localization to the pyrenoid (discussed in more details below). PGK1, GAP1, GAP3, FBA3, SBP1, RPE1, RPI1 and PRK1 proteins were located in the plastid stroma and not in the pyrenoid. While the two isoforms of GAPDH (GAP1 and GAP3) that are predicted to be localized to the chloroplast, indeed showed a strong Venus-signal in the stroma of this organelle, this was not true for the two isoforms of aldolase. The Venus-signal of FBA3 was found in the stroma but the Venus-signal of FBA2 was detected in the cytosol, in particular surrounding or confining the nucleus, indicating a role unrelated to the CBC.

Our pyrenoid-enrichment protocol detected 61.8% and 21.8% of Rubisco activity in the pyrenoid-enriched fraction of cells grown under LC and HC, respectively (Figure 2). The Venus-signals of the RBSC1 and RBSC2 subunits in the pyrenoid were very strong and very low in the stroma of non-dividing cells (Figure 3). The weaker stroma signal was dispersed over a much larger volume compared to the signal of the pyrenoid. Estimations by eye are therefore very difficult. Mackinder et al. (2016) quantified the fluorescence signal of RBSC1 and found 79% and 32% of the signal in pyrenoids in ambient-CO₂-grown cells and high-CO₂-grown cells, respectively. The lower values from the pyrenoid-enrichment protocol compared to fluorescence analyses might be because the pyrenoids were not completely stable during the enrichment protocol. Another possibility is that pyrenoids from dividing cells, which contain less Rubisco in their pyrenoid (Rosenzweig et al., 2017), contributed to a higher extent to the pyrenoid-enrichment analysis than to fluorescence analyses. However, the differences between the two approaches were less than 20%, which is not large considering these are from completely different methods, different laboratories and different cultivation set-ups. For our modelling approach, we took the values of the pyrenoid-enrichment protocols shown in Figure 2, because metabolites were measured in the same cultivation set-up.

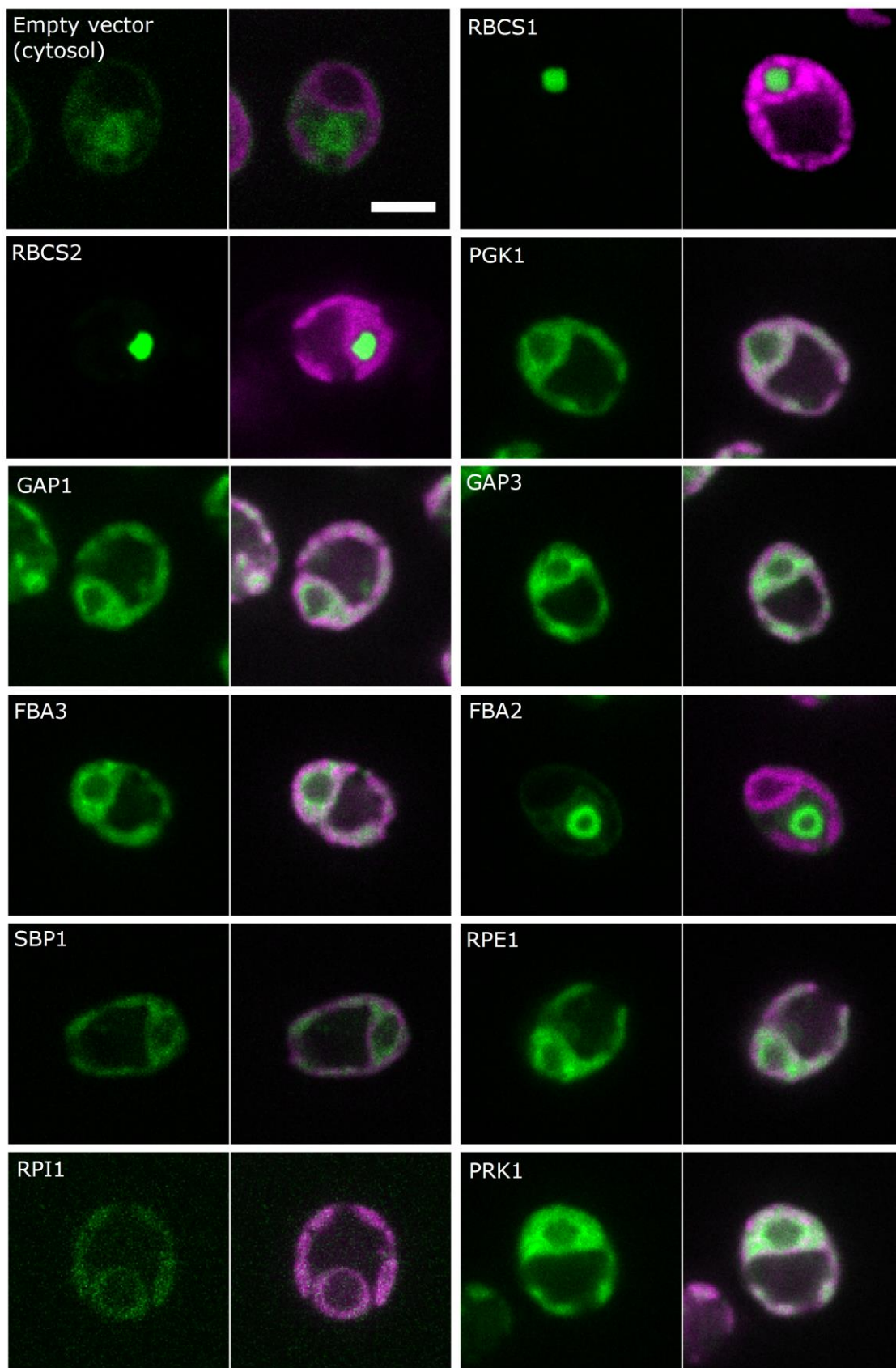


Figure 3. Localisation of CBC enzymes. *Chlamydomonas reinhardtii* CC-4533 cells expressing Venus-fusion constructs (green) were grown under ambient CO₂, imaged by fluorescence microscopy and two pictures per

constructs are shown. On the left side, solely the signal of the Venus-fusion construct (green) and on the right side, the overlay picture of the signal of the Venus-fusion construct (green) and the chlorophyll fluorescence (magenta) is shown. The white bar represents 5 μm . Details on the protein names are given in the text and Supplementary file 2.

Metabolites in high-CO₂ grown (HC) cells, and in low-CO₂ grown cells after 15 min of exposure to 5% CO₂ (LC*)

Absolute quantification of the metabolites of the CBC and starch synthesis were obtained using an ion-paired liquid-chromatography coupled to triple-quadrupole mass spectrometry (HPLC-MS/MS)-based approach (Figure 2, Supplementary file 1C). As treatments necessary to separate pyrenoid from stroma would affect metabolite levels, only the total amounts of metabolite could be quantified. To convert content per cell to concentration, whole cell volume was measured by a Coulter counter (Methods), and these were normalized to the chloroplast volume (31.18% of the whole cell volume) based on 3D reconstruction of EM-stacks of *C. reinhardtii* wild-type cells (Schotz, Bathelt, Arnold, & Schimmer, 1972) (Supplementary file 1D). Metabolite distributions between cytosol and chloroplast were estimated based on data obtained by non-aqueous fractionation (Gerhardt, Stitt, & Heldt, 1987) (Supplementary file 1D). Measurements were carried out on cells grown and harvested in high CO₂ (HC) and on cells grown in low CO₂ and bubbled with 5% CO₂ for 15 min before harvesting (LC*). This was done to investigate differences in metabolism between CCM-induced (LC*) and CCM-suppressed (HC) cells at comparable photosynthesis rates. This short high-CO₂ treatment of CCM-induced cell did not change the physiology of the cells as judged from an unchanged pyrenoid structure (Figure 2-figure supplement 1C). As anticipated, the rates of photosynthesis were almost equal in both sets of cells (55 and 57 $\mu\text{mol O}_2 \cdot \text{h}^{-1} \cdot \text{mg Chl}^{-1}$ for HC cells and for LC*, respectively; Supplementary file 1E). As this total flux remains the same between the two conditions, any differences in metabolite pools are likely due to physiological changes such as the altered distribution of Rubisco.

The LC* cells showed a significant (Student's *t*-test, *p*-value < 0.05) decrease in 3PGA, dehydroxyactone phosphate (DHAP) and significant increases in RuBP, fructose-6-phosphate (F6P), ribose-5-phosphate (R5P), xylulose-5-phosphate (Xu5P) and ribulose-5-phosphate (Ru5P) compared to HC cells (Figure 2, Supplementary file 1C). The increased level of RuBP and increased abundance of Rubisco in the pyrenoid under LC* provided a first indication that concentration gradient to drive diffusion or transport of RuBP into the pyrenoid may be increased in LC* cells. However, it remains unclear if and how the fluxes of the reactions comprising the CBC were affected by the microcompartments. For example, the significant decrease of 3PGA under low compared to high CO₂ could not be readily explained without considering a systems approach in which the effects of all participating components are jointly considered. Further, interpretation of the metabolite data needs to take the altered location of Rubisco into consideration (see above).

Modelling the effect of chloroplast microcompartmentation on the CBC

To investigate the effect of microcompartmentation on the organization and partitioning of the reaction fluxes and metabolite pools of the CBC, we devised a mathematical model tailored to *C. reinhardtii* (Methods, see Figure 4 for a graphical model representation and Supplementary file 3 for model details). The model consists of two nominal copies of the CBC, one in the stroma and a second one in the pyrenoid, interconnected by reversible transport reactions for every CBC intermediate. We combined the model with our experimental data to ask which parts of the CBC operate in the stroma, and which in the pyrenoid. For this purpose, the volume of the stroma and the pyrenoid were needed. The volume of the stroma was determined as described above and the pyrenoid volume was

calculated as the average of 12 and 10 TEM pictures of HC and LC cells of this study, respectively, applying the equation for the volume of an ellipsoid (Supplementary file 1F).

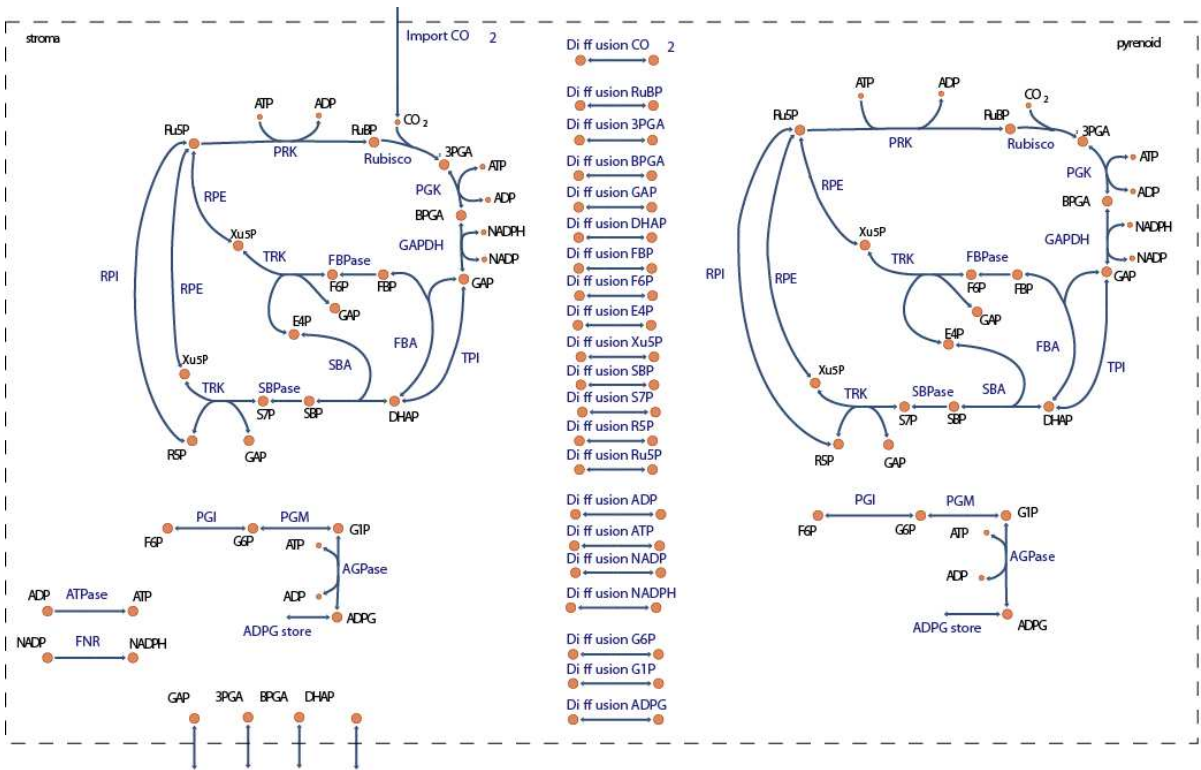


Figure 4. Graphical representation of the model for carbon fixation in *Chlamydomonas reinhardtii*. The model includes a copy of the Calvin-Benson cycle (CBC) in the chloroplast stroma and in the pyrenoid. In addition, the model considers reversible transport between the stroma and the pyrenoid for all CBC intermediates. A complete list of enzyme and metabolite names corresponding to the given abbreviations is presented in Supplementary file 3.

All enzymatic model reactions are decomposed into their elementary reactions i.e.; the formation of the substrate-enzyme complexes are explicitly considered (Methods). The resulting structure of the model was mathematically represented by the stoichiometric matrix, N , where rows correspond to model components (i.e., metabolites, enzymes, metabolite-enzyme complexes) and columns correspond to reactions (Orth, Thiele, & Palsson, 2010). The entries of matrix N indicated the molarity with which a component is produced (positive value) or consumed (negative value) by each reaction.

273 First, we sampled steady-state flux distributions, $v(c, k)$, from the flux cone, $C(N)$, given by
 274 $C(N) = \{v(c, k) | N \cdot v(c, k) = 0 \text{ and for every reaction } R_i, v_i(c, k) \geq 0\}$ of the modeled
 275 system under the additional constraint of constant CO_2 uptake ($398 \mu\text{M/s}$), ferredoxin-
 276 NADP+ reductase (FNR, $796 \mu\text{M/s}$) and ATPase activity ($1.194 \mu\text{M/s}$) representing
 277 invariant NADPH and ATP formation. In addition, we integrated protein abundances from
 278 our experimental data on protein distribution in the chloroplast for HC and LC cells to draw
 279 conclusions on the physiologically relevant part of the flux cone (see Methods) and to reduce
 280 the number of parameters which need to be estimated. The data were integrated under the
 281 assumption that the ratio of fluxes of the corresponding reactions between the stroma and the
 282 pyrenoid were bounded by the ratio of the experimentally-determined protein abundance (see
 283 Methods).

284 Next, we described the flux through each elementary reaction, v , by the ubiquitous mass
 285 action kinetics (Voit, Martens, & Omholt, 2015). According to this kinetic law, the flux
 286 through reaction R_i was expressed by $v_i = k_i \prod_j c_j^{\alpha_{ji}}$, with α_{ji} denoting the stoichiometry with
 287 which a component (i.e. enzyme or metabolite) j , of concentration c_j , enters reaction i as a
 288 substrate and k_i denoted the reaction rate constant. Log-transformation of this equation
 289 yielded a system of linear equations including the log-transformed fluxes, concentrations, and
 290 rate constants. Given a steady-state flux distribution sampled from $C(N)$ the linear system
 291 could be solved using a constraint-based optimization approach (see Methods) to obtain
 292 predictions of metabolite concentrations and rate constants under the constraint that the rate
 293 constants between stroma and pyrenoid were close to each other. For reactions with known
 294 rate constants, obtained from literature, the optimization program attempted to reduce the
 295 difference between predicted k_i and the respective literature values (Supplementary file 4A).
 296 This approach facilitated the investigation of multiple possible modes of action of the CBC
 297 based on complete sets of model parameters. The resulting model predictions provided

information about: (i) the flux state most compatible to data, (ii) microcompartment-specific metabolite and enzyme concentrations and (iii) rate constants serving as proxies for enzyme turnover rates k_{cat} .

Due to the ambiguous experimental data, with protein abundances indicating a low but detectable GAPDH and, sometimes, PRK activity in the pyrenoid fraction but low or non-detectable Venus-signal in the pyrenoid (Figures 2 + 3), we inspected model predictions for three different scenarios. We considered: (i) activity of PRK, Rubisco and GAPDH, (ii) activity of PRK and Rubisco, and (iii) only activity of Rubisco in the pyrenoid. To further reduce the number of parameters which need to be estimated, exchange was only allowed for metabolites involved in reactions catalyzed by enzymes present in the pyrenoid. To identify the best model, we used the Chi-square statistic, X^2 , between predicted and measured total concentration for 11 metabolites over 5,000 steady-state flux distributions (Figure 4-supplement 1). In line with the current understanding of the CCM, where apart from Rubisco, the remaining enzymes of the CBC are hypothesized to be situated in the stroma, a significant value for X^2 was obtained for the scenario in which Rubisco was the only active enzyme in the pyrenoid (average Rubisco localization in pyrenoid 61.8% for LC and 21.8% for HC conditions, $\bar{X}_{LC*}^2 = 2.20$, $\bar{X}_{HC}^2 = 0.52$). A significant value was also observed when the activities of PRK (average PRK localization in pyrenoid 1.2% for LC and 12.6% for HC conditions), Rubisco and GAPDH (average GAPDH localization in pyrenoid 7.8% for LC and 11% for HC conditions) were allowed ($\bar{X}_{LC*}^2 = 0.26$, $\bar{X}_{HC}^2 = 0.31$). Simulations of this latter scenario showed no activity of GAPDH in the pyrenoid, hence the good fit in the X^2 statistic was a result of allowing a circular transport of NADP, NADPH, BPGA and GAP. Circular transport of metabolites between stroma and pyrenoid, without metabolites being used in the pyrenoids, however, is physiologically unlikely. Under the assumption that PRK and Rubisco were active in the pyrenoid, we observed average X^2 values of $\bar{X}_{LC*}^2 = 74.15$,

$\bar{X}_{HC}^2 = 16.51$ (Figure 4-figure supplement 1). Hence, in the following, we only provide modelling results for the scenario with Rubisco as the only active enzyme in the pyrenoid. Since we obtained at least 1,000 samples with a significant fit between the predicted and measured concentrations under both experimental conditions, the presented findings rely on the parameter sets leading to the 1,000 best fits. In addition, we used the qualitative Pearson correlation coefficient to validate our predictions. We found that predicted quantities were in qualitatively excellent agreement with measurements under both conditions (Pearson correlation coefficient ≥ 0.99 , p-value $< 10^{-6}$, Figure 5). Therefore, we further used this model to investigate and understand the influence of microcompartmentation on the function of the CBC.

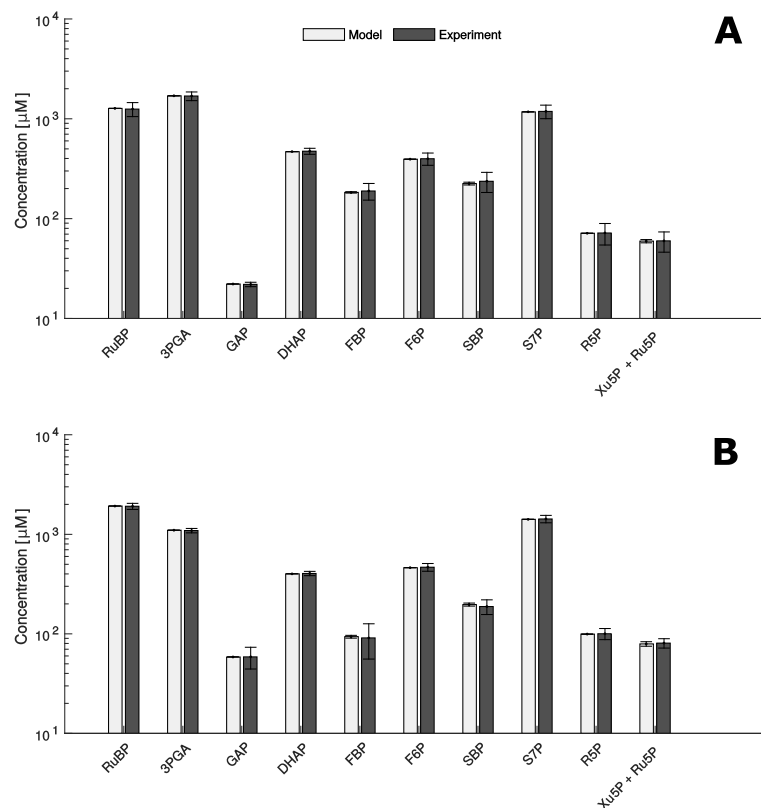


Figure 5. Comparison of metabolite data determined experimentally (Experiment) and by mathematical modelling (Model) under HC (A) and LC* (B) conditions. (A + B) Modelled data is shown as white bars (n =

1,000 \pm SD) and the SD-values are too small to be seen. Experimentally, metabolites were measured by HPLC-MS/MS as already shown in Figure 2 ($n = 4 \pm$ SD) (grey bars).

Two modes of CBC operation

Next, we investigated differences in thermodynamic characteristics in HC and LC* cells. We used the predicted metabolite concentrations and equilibrium constants, K_{eq} , obtained from eQuilibrator (Flamholz, Noor, Bar-Even, & Milo, 2012) to estimate $\Delta G = -RT * (\ln K_{eq} - \ln Q)$ for each reaction across the sampled flux distributions, where Q is the ratio of active product concentrations and active reactant concentrations. In LC* cells (CCM-induced) we found TRK to be the only enzyme operating in both directions (Figure 5-supplement 1). For the remaining enzymes, except RPE and RPI for which $\Delta G > 0$, the reactions were predicted to be exergonic (i.e., $\Delta G < 0$). The positive ΔG for reactions RPE and RPI may point to a substrate channeling (Chiappino-Pepe, Tymoshenko, Ataman, Soldati-Favre, & Hatzimanikatis, 2017). We observed a change in sign of ΔG between the two conditions for enzyme TPI only (Figure 5-figure supplement 1).

In addition, we studied the function of the CBC at the level of reaction fluxes. We compared the net flux, corresponding to the sum of fluxes of forward and backward reaction in case of reversible reactions for the HC and LC* cells (see Figure 6A for the fold-changes between the HC and LC* fluxes, see Figure 6-supplement 1 for the fluxes at HC and LC* separately, Supplementary file 5 + 6). Under the assumption that the rate of CO₂ uptake from the environment was the same in HC and LC* cells, the modelled rate of CO₂ diffusion into the pyrenoid for LC* cells showed a three-fold increase in comparison to HC cells, indicating that the model captures the function of the CCM (Figure 6B). The rate of the Rubisco reaction in the pyrenoid followed the CO₂ import into the microcompartment and was, therefore, three-fold increased under LC* conditions. Since the function of Rubisco depends

not only on the import of CO₂, but also on the availability of RuBP, its predicted rate of import into the pyrenoid from the stroma was also three-fold increased in LC* cells. In addition, the rate of 3PGA export from the pyrenoid into the stroma was higher under LC* conditions than in HC conditions.

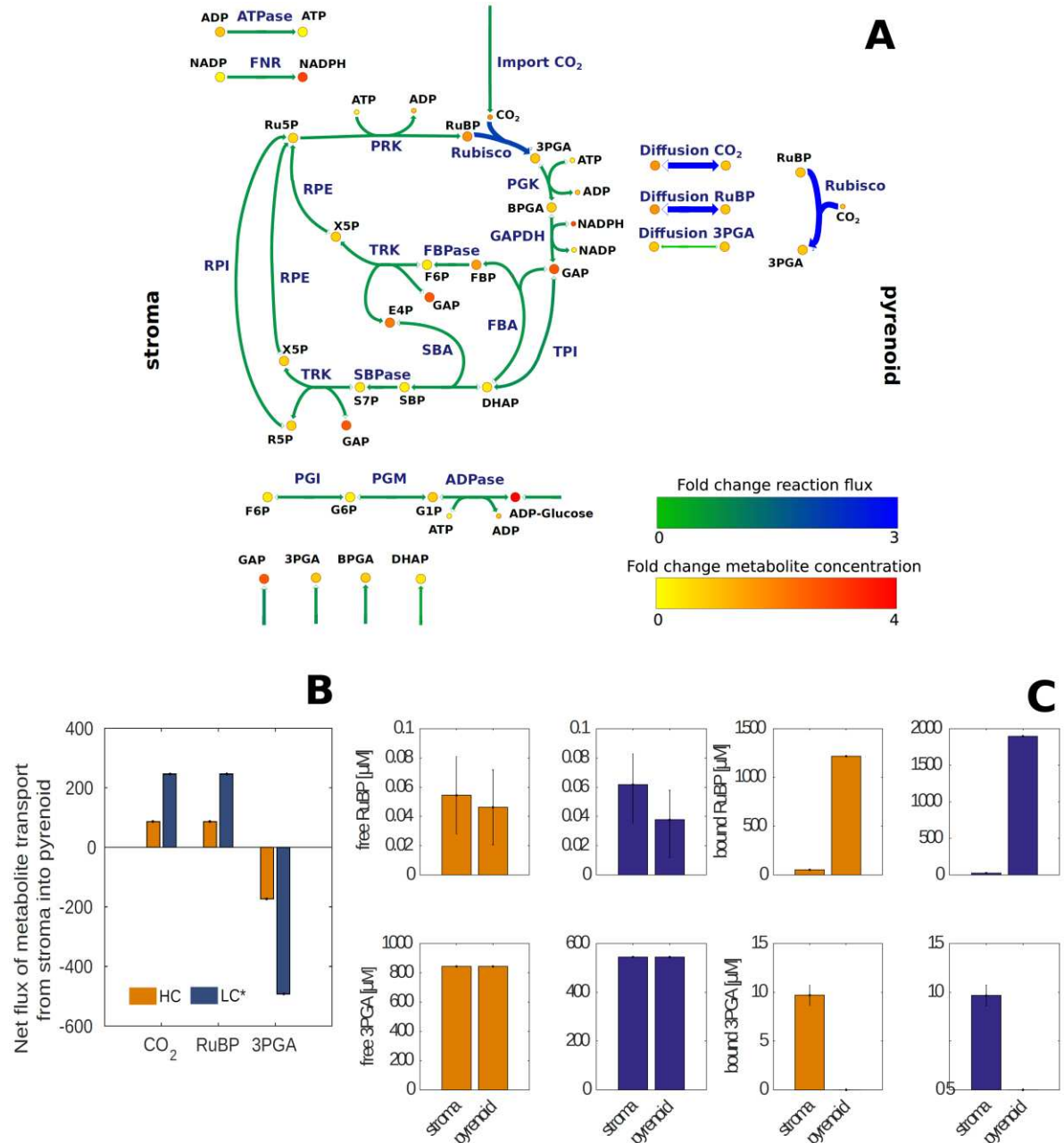


Figure 6. Changes in estimated reaction fluxes and metabolite concentrations for HC and LC* *Chlamydomonas reinhardtii* cells. (A) Fold changes of model predicted average net flux (represented by arrows) and total metabolite concentrations (represented by circles) between LC* and HC cells indicated by a colour code (see legend) and size of the arrows. The actual values are provided in Supplementary files 5 and 6 and summarized in Figure 6-source data 1. The main difference observed between HC and LC* conditions was

371 an increased flux through Rubisco in the pyrenoid and an increased flux of RuBP and 3PGA to the pyrenoid and
372 from the pyrenoid, respectively. The flux through the Calvin-Benson cycle located in the stroma, however, is
373 similar under both conditions (fold change of 1). (B) Net flux for transport of CO₂, RuBP and 3PGA between
374 stroma and pyrenoid under HC (orange) and LC* (blue) conditions. A positive value indicates transport from
375 stroma to pyrenoid, while a negative value indicates transport from pyrenoid into stroma. (C) Concentrations of
376 bound and free RuBP and 3PGA under HC (orange) and LC* (blue) conditions.

Mechanisms of metabolite transport between microcompartments

To examine the mode of transport between pyrenoid and stroma, the bound and free metabolite levels were determined for both conditions (Figure 6C, Supplementary files 5B and 6B). Due to elementary reactions considered in modelling (Methods), we predicted concentrations for free metabolites as well as concentrations for the respective metabolite-enzyme-complexes. In case a metabolite can bind multiple enzymes the concentration of the bound metabolite was given by the respective sum of concentrations over the respective enzymes. The model predicted that the vast majority of the RuBP was bound. The observed increase in RuBP concentration for LC* cells was therefore mainly due to an increase in bound RuBP in the pyrenoid as a result of an increased Rubisco concentration (Figure 6-source data 1). The model predicted slightly higher free RuBP in the stroma in comparison to the pyrenoid (0.024 μM and 0.008 μM difference under LC* and HC conditions, respectively). Furthermore, in line with increased transport RuBP rates into the pyrenoid, the difference between free RuBP in the stroma and pyrenoid was larger in LC* than HC cells. Since in both cell types we observed a concentration gradient in the direction of RuBP transport towards the pyrenoid, the model predictions indicate diffusion or facilitated transport may be a feasible mechanism of RuBP transport under HC and LC*, although the estimated concentration gradient is very small. In contrast, the model predicted equal free amounts of 3PGA between pyrenoid and stroma under HC and LC*, implying diffusional equilibrium.

DISCUSSION

Quantitative and qualitative experimental data were obtained for the distribution of CBC and starch synthesis pathway enzymes between the chloroplast stroma and the microcompartment pyrenoid, confirming that Rubisco is largely located in the pyrenoids (average Rubisco localization in pyrenoid 61.8% for LC and 21.8% for HC conditions). All other CBC enzymes were present at only very low amounts (PRK, GAPDH) or were totally absent from the pyrenoid in LC cells with an operational CCM. Metabolite data measured in whole cells revealed that LC* cells have altered CBC metabolite levels to those in HC cells at the same CO₂ concentration and net rate of photosynthesis. However, this data alone is not sufficient to understand flux between the stroma and pyrenoid.

A kinetic model, parametrizing each reaction in the stroma and pyrenoid, allowed us to calculate flux distributions under the two distinct physiological states. The validation of the model indicated statistically significant quantitative and qualitative agreement between the experimental and modelled chloroplast metabolite concentrations. The fit for the model as a whole was assessed, considering the contribution of the predictions for each metabolite level. The agreement between experimental data and predicted metabolite levels was statistically acceptable for 10 out of 16 individual metabolites. In the case of GAP and SBP, the lack of statistical fit could be due to the fact that these compounds are involved in redox-regulated reactions, namely the reduction of BPGA to GAP catalyzed by GAPDH (Sparla, Pupillo, & Trost, 2002) and the hydrolysis of SBP catalyzed by SBPase (Dunford, Durrant, Catley, & Dyer, 1998). The values given by the model are lower than the experimental pool sizes implying that there might be incomplete redox activation, which would decrease the full enzymatic . This discrepancy is in line with the fact that the model does not include redox regulation. This explanation is supported by the observation that the applied light intensity of 46 $\mu\text{mol photons}\cdot\text{m}^{-2}\cdot\text{s}^{-1}$ is not saturating, and analysis of SBP and S7P indicated that

SBPase is incompletely activated at this light intensity (Mettler et al., 2014). For the reaction catalyzed by GAPDH, it is likely that NADPH provided by the light reaction was rate limiting rather than GAPDH redox activation (Mettler et al., 2014).

To provide further validation of the model, we compared the predicted rate constants with values for k_{cat} available from literature that were not used in the model parameterization (Methods; Supplementary file 4A). This was the case for TRK (Xu5P, rate constant = 37 s^{-1} ; Ru5P, rate constant = 37 s^{-1}) (Supplementary file 4B) for which the published k_{cat} values in spinach are $< 0.02 \text{ s}^{-1}$ for Xu5P and Ru5P (Teige, Melzer, & Suss, 1998). The values for the plant TRK reported in literature are surprisingly low, since those in yeast ($k_{\text{cat}} = 113 \text{ s}^{-1}$) and human ($k_{\text{cat}} = 9 \text{ s}^{-1}$) (Albe, Butler, & Wright, 1990) are much higher.

The first important output of the model included the fluxes of the exchange reactions between the pyrenoid and the stroma. The mathematical model enabled us to calculate exchange fluxes between chloroplast stroma and pyrenoid based on enzyme partitioning, rate constants of enzymatic reactions and steady-state metabolite levels. The model predicted an increase in the flux of the Rubisco reaction inside the pyrenoid under LC* compared to HC conditions. This prediction reflects the increased presence of Rubisco in the pyrenoid under these conditions. The model also predicted import of RuBP and export of 3PGA into and from pyrenoid, respectively, with both fluxes being higher under LC* compared to HC conditions. The concentration gradient for RuBP between stroma and pyrenoid was larger under LC* than under HC, but for both conditions the concentration gradients were small ($0.024 \mu\text{M}$ and $0.008 \mu\text{M}$, respectively). For 3PGA, the model predicted, for both conditions, that there is no concentration gradient between stroma and pyrenoid. Since there is no accumulation of RuBP in the pyrenoid or 3PGA in the stroma, active transport seems unnecessary and movement between the microcompartments may occur by diffusion.

Previously, the starch sheath surrounding the pyrenoid under ambient but not under high CO₂ conditions, was suggested to work as diffusional barrier to prevent CO₂ from diffusing out of the pyrenoid (Badger & Price, 1994). In this case, the starch sheath would also represent a diffusional barrier for RuBP entering into the pyrenoid. In the model, such an increased diffusional barrier could be seen as a change in the diffusion constant between HC, where no starch sheet was present, and LC*, where a starch sheet was established. The diffusion constants is proportional to 10,623 s⁻¹ (86.664 μM s⁻¹ * 0.008158⁻¹ μM⁻¹) and 10,259 s⁻¹ (246.12 μMs⁻¹ * 0.02399⁻¹ μM⁻¹) for HC and LC*, respectively (Figure 6A, Supplemental file 7), revealing that the difference in the diffusion constants was minor. Therefore, our model does not support the idea of an increased diffusional barrier between pyrenoid and stroma under LC* for RuBP. This finding is experimentally supported by the fact that a starch-less mutant, also lacking the starch sheath around the pyrenoid, is still able to develop a fully functional CCM (Villarejo et al., 1996).

As the fluxes of both 3PGA and RuBP are increased under LC* compared to HC with minor (RuBP) or no (3PGA) increase in the concentration gradients, flux is increasing with minor or no change in the driving force. This implies that there instead of a strong diffusional boundary there may be facilitated diffusion under LC* compared to HC. Recently, several proteins that are known to be expressed under low CO₂ conditions but are of unknown function were sub-cellularly localized (Mackinder et al., 2017). LCIC / LCIB and LCI9 are expressed in the proximity of the starch sheath and surrounding the pyrenoid, which is consistent with one or several of these proteins being involved in facilitating diffusion of RuBP into and of 3PGA out of the pyrenoid. This would occur exclusively under low CO₂ conditions, as the according genes are only expressed under low CO₂ (Yamano, Miura, & Fukuzawa, 2008; Yamano et al., 2010). Recently it was suggested that LCIC / LCIB most

likely has a carbonic anhydrase activity (Jin et al., 2016), but additional functions are still possible.

A high resolution cryoEM study of the *C. reinhardtii* chloroplast (Engel et al., 2015) revealed the presence of pyrenoid minitubules that form narrow continuous channels between the inter-thylakoid stromal space and the pyrenoid matrix. One function of these minitubules could be to facilitate diffusion of RuBP and 3PGA, apart or in addition to the protein candidates mentioned above. The estimated minitubule lumen diameter is of the order of 3-4 nm by 8-15 nm, which is not much larger than the longest axes of RuBP and 3PGA (about 1.2 nm and 0.7 nm, respectively), so diffusion of these metabolites in the minitubules would be possible. It will be interesting to learn if the physiochemical properties of these minitubules favor facilitate diffusion of these metabolites, either as free acids or as the magnesium complexes that are likely to predominate at pH and magnesium concentration found in the stroma in the light (Portis, 1981; Werdan, Heldt, & Milovancev, 1975). Charge properties might, speculatively, provide a means to discriminate between CBC intermediates and the weakly anionic bicarbonate and neutral CO₂.

Under low CO₂ conditions and a fully functional CCM, the limiting Rubisco substrate CO₂ is concentrated in the pyrenoid. Moreover, our data indicate that the CCM also establishes structures that allow facilitated transport of RuBP, the other Rubisco substrate, from the stroma to the pyrenoid and the release of the Rubisco product 3PGA into the stroma, where the rest of the CBC enzymes are located. Such channels for exchange of CBC metabolites were suggested to be present in the pyrenoid of *C. reinhardtii* (Engel et al., 2015) and the proteinaceous shell of the carboxysome based on the number of shell proteins and their localization in the shell (Kerfeld & Melnicki, 2016). However, supporting experimental data to our knowledge is scarce so far and therefore our study is the first with underlying

experimental metabolite data postulating such transport reactions in a carbon-concentrating microcompartment.

Altogether, our systems biology approach allowed us to demonstrate (i) that changes in microcompartments cause specific inhomogeneities that affect steady-state metabolite levels and have to be considered in mathematical modelling approaches based on such experimental data; (ii) that mathematical models with mild assumptions can be used to study flux distributions between reactions inside and outside microcompartments, which are very difficult and often technically impossible to study experimentally; and (iii) that metabolites can be identified that are exchanged between the compartments and their exchange fluxes quantified. Our study opens the possibility to study the effects of microcompartmentation in different cellular scenarios and to understand their role in the overall physiology of the investigated system.

MATERIALS AND METHODS

Key Resources Table

Reagent type (species) or resource	Designation	Source or reference	Identifiers	Additional information
strain, strain background (<i>Chlamydomonas reinhardtii</i>)	CC1690 wild-type strain	Chlamydomonas Resource Center	RRID:SCR_014960	
strain, strain background (<i>Chlamydomonas reinhardtii</i>)	CC-4533 wild-type strain	Chlamydomonas Resource Center	RRID:SCR_014960	-
antibody	rabbit Anti-Beta-CA1	AgriSera	Cat# AS111737; RRID:AB_10752086	(1:7500)
antibody	rabbit Anti-AtpD	AgriSera	Cat# AS101590; RRID:AB_10754669	(1:30000)
software, algorithm	MaxQuant	MaxQuant (http://www.biochem.mpg.de/5111795/maxquant)	RRID:SCR_014485	version 1.5.2.8
software, algorithm	Codes used for modelling			The mathematical models can be accessed via github at: https://github.com/ankueken/Chlamy_model

Cell growth

Chlamydomonas reinhardtii CC1690 wild-type strain (Sager, 1955) was obtained from the Chlamydomonas Resource Center (RRID:SCR_014960) and cultivated as described in Mettler et al. (2014). Cells were growth photoautotrophically in a 5-litre bioreactor BIOSTAT®B-DCU (Sartorius Stedim, Germany) for five days until a cell density of $3\text{-}5 \times 10^6$ cells*ml⁻¹ was reached and thereafter, turbidity was kept constant. The culture in the

bioreactor was constantly stirred with 50 rpm at 24°C, exposed to an average of 46 $\mu\text{mol photons}\cdot\text{m}^{-2}\cdot\text{s}^{-1}$ (measured internally at four different positions) and bubbled at a rate of 400 ccm with air enriched with 5% CO_2 . Turbidity was kept constant by medium exchange (125 $\text{ml}\cdot\text{h}^{-1}$) for two days before harvesting the high- CO_2 -grown cells. Then the air bubbling of the bioreactor was changed from 5% CO_2 to ambient air. Cells were adapted to the low- CO_2 conditions for 30 h. Turbidity was kept constant by medium exchange (39 $\text{ml}\cdot\text{h}^{-1}$) and CO_2 in the outlet air of the bioreactor was measured (Figure 2-figure supplement 1). The CO_2 level measured by gas chromatography in the outlet air of the bioreactor dropped within 12 h from 4.5% (bubbling with 5%) to a constant 0.02% (bubbling with air of approximately 0.039% CO_2). Levels inducing CCM (0.1%) were already reached after 4 h but the system needed at least an additional 8 h to equilibrate at 0.02% CO_2 . We can therefore assume that cells in the bioreactor are exposed to, at a maximum, 0.02% CO_2 . LC cells were harvested after 30 h of bubbling with ambient air and LC* cell after an additional 15 min bubbling with air enriched with 5% CO_2 . Cell number and cell volume were determined by a Z2™ Cell Coulter® (Beckman Coulter, USA) in triplicates of 100-fold diluted samples.

Cell harvesting

Before harvesting, 500 ml of, both, the high- and the low- CO_2 -grown cells were transferred to a 1-L glass bottle and kept at the same light intensity (46 $\mu\text{mol photons}\cdot\text{m}^{-2}\cdot\text{s}^{-1}$, measured internally as indicated above) as in the bioreactor, stirred and bubbled with ambient (LC) or 5% CO_2 (HC and LC*) for 15 min. For metabolite measurement, the cells were quenched with 70% cold methanol as described in Mettler et al. (2014). For enzyme activities and proteomics experiments, 10 ml of cells were spun-down at 4000 rpm for 2 min at 4°C and stored at -80°C before usage.

538

539 **Metabolite measurements by HPLC-MS/MS**

540 Polar metabolites were extracted with chloroform/methanol/water, separated with an ion-
541 paired liquid chromatography and detected on a triple quadrupole as described in Mettler et
542 al. (2014). The absolute amounts of metabolites measured by HPLC-MS/MS were
543 normalized to the cell volume determined by a Coulter counter described above. The
544 metabolite levels were then normalized to the chloroplast volume according to Schotz et al.
545 (1972) using distributions between cytosol and chloroplast according to Gerhardt et al.
546 (1987). See Supplementary file 1D and the Result section for more details.

547

548 **Enzymatic activities**

549 The ten ml algal material was defrosted on ice and extracted with extraction buffer (EB)
550 containing 2% Triton (50 mM HEPES, 20 μ M leupeptin, 500 μ M DTT, 1 mM PMSF, 17.4%
551 glycerol). The samples were sonicated 3 x 15 s (6 cycles, 50% intensity, Sonoplus Bandelin
552 electronics, Germany) and kept on ice in between for 90 s. Half of the sample was then used
553 for analysis of total enzyme activity and half was centrifuged at 14000 rpm for 2 min to
554 obtain a soluble and pellet fraction. The pellet was washed twice with 500 μ l EB before
555 resuspension in 500 μ l EB. The enzyme activities of total, soluble and pellet fraction were
556 analyzed together in 96 well microplates using a Janus pipetting robot (Perkin-Elmer,
557 Belgium) and absorbances were determined using a Synergy, an ELX-800 or an ELX-808
558 microplate reader (Bio-Tek, Germany). For each enzyme three different dilutions of each
559 algal sample were measured (final concentrations in assay were 1:60, 1:300, 1:600). The
560 AGPase (Gibon et al., 2004), PGM (Manjunath, Lee, VanWinkle, & Bailey-Serres, 1998) and

Rubisco (Sulpice et al., 2007) enzymatic assay were performed as described previously. For Rubisco activity measurement, the assay length was adjusted to 30-60 min.

Proteomics data

The soluble and pellet fractions described above were subjected to shotgun proteomics analysis as described in Mackinder et al. (2016). Data analysis was done using the MaxQuant Software (RRID:SCR_014485) (Cox & Mann, 2008).

Protein localization

Proteins were tagged and sub-compartmentally localized as described in Mackinder et al. (2017). Briefly, for the fluorescence protein tagging, open reading frames of CBC genes were PCR amplified (Phusion Hotstart II, Thermo Fisher Scientific, U.S.A.) from genomic DNA, gel purified and cloned in-frame with a C-terminal Venus-3xFLAG (pLM005) tag (Mackinder et al., 2016) by Gibson assembly. Junctions were Sanger sequenced and constructs were linearized by either EcoRV or DraI prior to transformation into WT *C. reinhardtii* (CC-4533). For transformation by electroporation, 14.5 ng kbp-1 of cut plasmid was mixed with 250 μ L of 2×10^8 cells mL^{-1} at 16 °C in a 0.4 cm gap electroporation cuvette then transformed using a Gene Pulser II (Bio-Rad Laboratories, U.S.A.) set to 800V and 25 μ F. Transformed cells were selected on Tris-acetate-phosphate (TAP) paromomycin (20 μ g mL^{-1}) plates and maintained in low light (5-10 $\mu\text{mol photons m}^{-2} \text{s}^{-1}$) until screening for fluorescence using a Typhoon Trio fluorescence scanner (GE Healthcare, U.S.A.).

For confocal microscopy, Venus-tagged lines were grown photoautotrophically in Tris-phosphate (TP) liquid medium in air (ambient CO_2) at 150 $\mu\text{mol photons m}^{-2} \text{s}^{-1}$ light

intensity. 15 μL of cells at $\sim 2\text{--}4 \times 10^6$ cells mL^{-1} were pipetted onto poly-L-lysine coated plates (Ibidi) and overlaid with 120 μL of 1% TP low-melting-point agarose at $\sim 34^\circ\text{C}$ to minimize cell movement. Images were acquired using a spinning-disk confocal microscope (Leica DMI6000, Leica Microsystems, Germany). Venus signal was detected by 514 nm excitation with 543/22 nm emission and chlorophyll using 561 nm excitation with 685/40 nm emission. Images were analyzed using Fiji (Schindelin et al., 2012).

Model description

The model was constructed to simulate carbon fixation in the chloroplast under different CO_2 availability. The model included two compartments: (i) the chloroplast stroma and (ii) the pyrenoid, a microcompartment located inside the chloroplast associated with the operation of a CCM. The postulated function of the pyrenoid is to generate a CO_2 -rich environment around the photosynthetic enzyme Rubisco (Kuchitsu et al., 1988b, 1991). During carbon fixation Rubisco catalyses the production of two molecules 3PGA from RuBP and CO_2 . Moreover, it catalyses the first reaction of the photorespiratory pathway: the reaction of RuBP and oxygen (O_2) to 3PGA and 2-phosphoglycolate. The model, however, did not include this reaction since under the high CO_2 conditions, this reaction was very likely suppressed (Supplementary file 1E).

To investigate the role and interplay of the pyrenoid and the CBC we included two full copies of the CBC, one in the chloroplast stroma and one in the pyrenoid. The copies of the CBC were linked by reversible transport reactions for all CBC intermediates. The enrichment of CO_2 in the pyrenoid (CCM) can be achieved via diffusion of CO_2 from the stroma into the pyrenoid. A full list of model reactions and components is presented in Supplementary file 2.

Model construction

608 The model simulated carbon fixation on the chloroplast level and included 62 reactions
 609 distributed over the chloroplast stroma and the pyrenoid. To compare the simulated data and
 610 experimentally determined enzyme parameters, each reaction was modelled by its elementary
 611 reaction steps. More specifically, given an irreversible reaction $A \rightarrow B$ catalyzed by enzyme
 612 E , the model included three elementary reactions: $A + E \leftrightarrow AE$ and $AE \rightarrow B + E$. For
 613 reversible reactions $C \leftrightarrow D$ the model includes six elementary reactions $C + E \leftrightarrow CE$,
 614 $CE \rightarrow D + E$, $D + E \leftrightarrow DE$ and $DE \rightarrow C + E$.

615 After splitting of reactions the model consists of 226 irreversible reactions and 128
 616 components (metabolites, enzymes, enzyme-substrate complexes). Each CBC copy, thereby,
 617 comprised 65 elementary reactions linked by 40 irreversible diffusion reactions. Moreover,
 618 the model included eight irreversible reactions transporting triose-phosphates from the stroma
 619 into the cytosol and vice versa, ATPase reaction converting ADP to ATP and a simplified
 620 ferredoxin-NADP+ reductase (FNR) reaction converting NADP to NADPH. The production
 621 of NADPH and ATP were calculated from the measured production of oxygen, assuming two
 622 molecules of NADPH produced per oxygen molecules and 1.5 ATP molecules per NADPH
 623 molecule (Supplementary File 1G).

624 The underlying system of ordinary differential equations (ODE), therefore, simulated a
 625 system of $n = 226$ reactions acting on $m = 128$ model species and was formulated as
 626 $\frac{dc_i}{dt} = \sum_{j=1}^m n_{ij} v_j$, where v_j was the flux through reaction j and n_{ij} the respective
 627 stoichiometric coefficient in the stoichiometric matrix N , indicating the molarity with which
 628 substrate i enters reaction j . The ODE system was used to simulate the steady-state
 629 concentrations c of all model species under different environmental conditions by solving
 630 $\frac{dc_i}{dt} = \sum_{j=1}^m n_{ij} v_j = 0$. The reaction flux $v(c, k)$ depended on species concentrations c and
 631 reaction rate constants, k , and is calculated using the law of mass-action. Thus, the flux

through an irreversible reaction j was given by $v_j(c, k) = k_j \prod_i c_i^{n_{ij}^-}$, where $n_{ij}^- = -n_{ij}$ if $n_{ij} < 0$ and 0, otherwise.

Model parameterization

Here, we describe the procedure of determining parameter values for c and k for sampled flux distributions, v .

To guarantee a steady state, we first sampled steady-state flux distributions with the COBRA Toolbox (Schellenberger et al., 2011) function *sampleCbModel* by sampling solutions of the linear program in Eq. (1). To obtain flux distributions leading to a high quality fit between simulated and measured data and to reduce the number of parameters which need to be estimated, we integrated the measured enzyme distribution between stroma and pyrenoid, whereby the flux ratio between pyrenoid and stroma for a reaction catalyzed by enzyme E follows the measured ratio of protein abundance. Therefore, we sampled flux distributions from the solution space of the following linear program:

$$\begin{aligned}
 Nv &= 0 \\
 v_{pyrenoid} &= q(v_{stroma} + v_{pyrenoid}) \\
 v^{FNR} &= 796 \\
 v^{ATPase} &= 1.194 \\
 v^{CO2\ uptake} &= 398 \\
 0 &\leq v \leq v_{max}
 \end{aligned} \tag{1}$$

Consequently, if $e_{pyrenoid} = q(e_{stroma} + e_{pyrenoid})$, where e was the measured relative enzyme activity or if available amount, then $v_{pyrenoid} = q(v_{stroma} + v_{pyrenoid})$. While q was chosen uniformly at random for each sampled flux distribution from the measured range.

649 For enzymes with measured relative activity in the pyrenoid below 5%, we considered only
 650 the enzyme located in the stroma to be active. In addition, based on experimental data we
 651 fixed the rate of CO₂ uptake to 398 μM/s. As upper limit of flux through a reaction we used
 652 $v_{max} = 1,000 \mu\text{M/s}$. Moreover, we fixed the flux through FNR and ATPase to constant
 653 values estimated from experimental data since light intensity was unaltered.

654 For each flux distribution v^* obtained from sampling, we determined species concentrations c
 655 and reaction rate constants k leading to the respective flux distribution under mass-action
 656 kinetics by solving the program in Eq. (2):

$$\begin{aligned} & \min \varepsilon^+ + \varepsilon^- \\ & \forall_{j=1:n} \end{aligned} \tag{2}$$

$$\log v_j^* = \log k_j + \sum_{i=1}^m n_{ij}^- \log c_i$$

$$\log k_{pyrenoid} - \log k_{stroma} + \varepsilon^+ = 0$$

$$\log k_{pyrenoid} - \log k_{stroma} - \varepsilon^- = 0$$

$$\log k_{min} \leq \log k \leq \log k_{max}$$

$$\log c_{min} \leq \log c \leq \log c_{max}$$

$$\varepsilon^+ \geq 0, \varepsilon^- \geq 0.$$

658 Since we assumed that k depends not only on environmental parameter, like temperature and
 659 pressure, but also includes regulation, which cannot be integrated in mass-action kinetics
 660 (e.g., allosteric regulation), we asked for the minimum difference in k between pyrenoid and
 661 stroma leading to a feasible solution of the program. For reactions with known enzymatic
 662 turnover obtained from BRENDA (Chang et al., 2015) (Supplementary file 3), we integrated

this information by restricting the respective parameter boundaries. Since the model provides subcompartment-specific estimates of metabolite concentrations, we considered the sum of the respective stroma and pyrenoid metabolite concentrations and compared them to the estimated and measured metabolite concentrations in the chloroplast. We then determined the goodness-of-fit for each set of simulated metabolite concentrations and enzyme distribution and rank the parameter sets based on their chi-square value considering the 1,000 top ranked for further investigation.

Net flux calculation

In case of non-enzymatic reactions of form $A \xrightleftharpoons[v_b]{v_f} B$ the reported net flux was calculated as

$v_f - v_b$. Since the activity of an enzyme is given by the rate of product formation per unit of time, we consider reaction flux v_{cat} as net flux for an irreversible reaction catalyzed by

enzyme E with elementary reactions $A + E \xrightleftharpoons[v_b]{v_f} AE$ and $AE \xrightarrow{v_{cat}} B + E$. In case of reversible

enzymatic reactions modelled by elementary reactions $C + E \xrightleftharpoons[v_{b1}]{v_{f1}} CE$, $CE \xrightarrow{v_{cat,f}} D + E$,

$D + E \xrightleftharpoons[v_{b2}]{v_{f2}} DE$ and $DE \xrightarrow{v_{cat,b}} C + E$, we consider $v_{cat,f} - v_{cat,b}$ as reported net flux.

ACKNOWLEDGEMENTS

We thank Joost van Dongen for the usage of equipment for photosynthesis rate measurements and Marc-Aurel Schöttler and Arren Bar-Even for critical reading. AK acknowledges support by the Max Planck Society and TM-A acknowledges support by the Deutsche

Forschungsgemeinschaft (EXC 1028). FS, MSt, MSch, and TM-A acknowledge support by the Federal Ministry of Education and Research (BMBF), Germany, within the frame of the GoFORSYS Research Unit for Systems Biology (FKZ0313924). MJ acknowledges support by the National Science Foundation (EF-1105617), the National Institutes of Health (DP2-GM-119137), and the Simons Foundation and HHMI (55108535).

COMPETING INTEREST

The authors declare that no competing interests exist.

SUPPLEMENTAL DATA

Supplementary file 1. Experimental data.

Supplementary file 2. Protein information for Venus localization.

Supplementary file 3. Model structure.

Supplementary file 4. Predications of k_{cat} -values compared to literature values.

Supplementary file 5. Raw data of the model for HC conditions.

Supplementary file 6. Raw data of the model for LC* conditions.

Figure 6-source data 1. Summary of the most important concentrations and fluxes.

FIGURE LEGENDS

Figure 1. Simplified scheme of CBC cycle with and without carbon-concentrating mechanism (CCM) in *Chlamydomonas reinhardtii*. Under high CO₂ conditions, no CCM is established (A). After exposure to ambient CO₂, a CCM is induced (B). As most of Rubisco and the other CBC enzymes are in the stroma under high CO₂, most CBC flux is in the stroma (big grey circle in the stroma) and only partly involves the pyrenoid (smaller grey circle) (A). As most of Rubisco is inside the pyrenoid under ambient CO₂, the CBC requires movement of selected metabolites between the stroma and pyrenoid (big grey circle) (B). To find out the exact differences of flux distribution between stroma and pyrenoid under these two conditions and how metabolites are exchanged between the two microcompartments were the aims of this study. Scheme adapted and simplified from Borkhsenius et al. (1998), Moroney et al. (2011), Wang et al. (2011), Engel et al. (2015) and Mackinder et al. (2016).

Figure 2. Experimental data for protein distributions (outer yellow circle) and metabolite concentrations (inner blue circle) in CCM-suppressed (white bars, HC) and CCM-induced (grey bars, LC for proteins and LC* for metabolites) conditions. *Chlamydomonas reinhardtii* CC1690 cells were grown under high CO₂ (HC for proteins and metabolites; white bars), ambient CO₂ (LC for proteins; grey bars) and ambient CO₂ bubbled for 15 min with high CO₂ (LC* for metabolites; grey bars). Enzyme distribution between a pyrenoid-enriched fraction (P) and a stroma-enriched fraction (S) was determined by enzyme activity measurements (Rubisco; $n = 4 \pm \text{SE}$) and shotgun proteomics (all other proteins; $n = 4 \pm \text{SE}$). Metabolites of the Calvin-Benson cycle (CBC) in total cells were measured by HPLC-MS/MS. The metabolite concentrations were normalized to the chloroplast volume as described in the Result section and Supplementary file 1D, and given as absolute concentrations (μM) in the chloroplast, which includes both microcompartments, the stroma and the pyrenoid ($S + P$) ($n = 4 \pm \text{SE}$). Student's *t*-test ($\alpha = 0.05$), significantly changed metabolites are marked with one asterisk.

Figure 2-figure supplement 1. Induction of carbon concentrating mechanism (CCM).

Chlamydomonas reinhardtii CC1690 were grown at $46 \mu\text{mol photons} \cdot \text{m}^{-2} \cdot \text{s}^{-1}$, 24°C and bubbled with 5% CO₂ (HC) for two days at constant turbidity in a bioreactor. CO₂ in the outlet air of the bioreactor was measured continuously during a 48 h run (A). From time point

zero onwards the culture was aerated with ambient air (0.039% CO₂). The inserted graph shows the same CO₂ data at lower CO₂ concentrations. Cultures were harvested before (HC) and 25 and 34 h (LC) after low-CO₂ exposure for Western blot analysis (B). Protein amounts equivalent to 1 µg chlorophyll were loaded per lane and separated by 12% SDS-PAGE before transferred to a nitrocellulose membrane for detection via chemiluminescence by an antiserum recognizing mtCA (AgriSera Cat# AS11 1737, RRID:AB_10752086). Loading control: CF₁β, β-subunit of the CF₁-component of CF₁F₀-ATP synthase AgriSera Cat# AS10 1590, RRID:AB_10754669). Transmission electron microscopy (TEM) of cells exposed for 30 h to low CO₂ and 15 min to high CO₂ (LC*; C). Cells were then quenched in the light for metabolite analysis by LC-MS/MS. Measure bar = 2 µm.

Figure 3. Localisation of CBC enzymes. *Chlamydomonas reinhardtii* CC-4533 cells expressing Venus-fusion constructs (green) were grown under ambient CO₂, imaged by fluorescence microscopy and two pictures per constructs are shown. On the left side, solely the signal of the Venus-fusion construct (green) and on the right side, the overlay picture of the signal of the Venus-fusion construct (green) and the chlorophyll fluorescence (magenta) is shown. The white bar represents 5 µm. Details on the protein names are given in the text and in Supplementary file 2.

Figure 4. Graphical representation of the model for carbon fixation in *Chlamydomonas reinhardtii*. The model includes a copy of the Calvin-Benson cycle (CBC) in the chloroplast stroma and in the pyrenoid. In addition, the model considers reversible transport between the stroma and the pyrenoid for all CBC intermediates. A complete list of enzyme and metabolite names corresponding to the given abbreviations is presented in Supplementary file 3.

Figure 4-figure supplement 1. Distribution of Chi-square statistic for 5,000 sampled steady-state flux distributions under three different assumptions. Model predictions under non-CCM (HC, A) and CCM-induced (LC*; B) conditions were validated using the Chi-square statistic between predicted and measured total concentration for 11 metabolites over 5,000 sampled steady-state flux distributions. The validation was done under three different assumptions: (i) activity of PRK, Rubisco and GAPDH, (ii) activity of PRK and

Rubisco, and (iii) only activity of Rubisco in the pyrenoid. The red line shows the Chi-square statistic corresponding to a significance level of 0.05.

Figure 5. Comparison of metabolite data determined experimentally (Experiment) and by mathematical modelling (Model) under HC (A) and LC* (B) conditions. (A + B) Modelled data is shown as white bars ($n = 1,000 \pm \text{SD}$) and the SD-values are too small to be seen. Experimentally, metabolites were measured by HPLC-MS/MS as already shown in Figure 2 (grey bars, $n = 4 \pm \text{SD}$).

Figure 5-figure supplement 1. Distribution of estimated ΔG values for CBC metabolites over 1,000 sampled steady-state flux distributions under no-CCM (HC; A) and CCM-induced (LC*; B) conditions. The estimated ΔG was negative for all enzymes except RPE and RPI for which $\Delta G > 0$. In addition, TRK was found to be the only enzyme operating in both directions.

Figure 6. Changes in estimated reaction fluxes and metabolite concentrations for HC and LC* *Chlamydomonas reinhardtii* cells. (A) Fold changes of model predicted average net flux (represented by arrows) and total metabolite concentrations (represented by circles) between LC* and HC cells indicated by a colour code (see legend) and size of the arrows. The actual values are provided in Supplementary files 5 and 6 and summarized in Figure 6-source data 1. The main difference observed between LC* and HC conditions was an increased flux through Rubisco in the pyrenoid and an increased flux of RuBP and 3PGA to the pyrenoid and from the pyrenoid, respectively, for LC* cells. The flux through the Calvin-Benson cycle located in the stroma, however, is similar under both conditions (fold change of 1). (B) Net flux for transport of CO_2 , RuBP and 3PGA between stroma and pyrenoid under HC (orange) and LC* (blue) conditions. A positive value indicates transport from stroma to pyrenoid, while a negative value indicates transport from pyrenoid into stroma. (C) Concentrations of bound and free RuBP and 3PGA under HC (orange) and LC* (blue) conditions.

Figure 6-figure supplement 1. Reaction flux estimated for *Chlamydomonas reinhardtii* cells grown under non-CCM (HC; A) and CCM-induced (LC*; B) conditions. The average values of the flux and total metabolite concentration are indicated by a colour code (see legend) and size of the arrows (denoting the reactions). The actual values are provided in Supplementary files 5 and 6. The main difference observed between HC and LC* conditions was an increased flux through Rubisco in the pyrenoid under LC* and an increase in the flux of RuBP and 3PGA into the pyrenoid and from the pyrenoid, respectively, under LC*. The flux through the Calvin-Benson cycle located in the stroma, however, was similar under both conditions.

References

- Albe, K. R., Butler, M. H., & Wright, B. E. (1990). Cellular Concentrations of Enzymes and Their Substrates. *Journal of Theoretical Biology*, 143(2), 163-195. doi:10.1016/S0022-5193(05)80266-8
- Badger, M. R., & Price, G. D. (1994). The Role of Carbonic-Anhydrase in Photosynthesis. *Annual Review of Plant Physiology and Plant Molecular Biology*, 45, 369-392.
- Bazylinski, D. A., & Frankel, R. B. (2004). Magnetosome formation in prokaryotes. *Nat Rev Microbiol*, 2(3), 217-230. doi:10.1038/nrmicro842
- Berry, S., Fischer, J. H., Kruip, J., Hauser, M., & Wildner, G. F. (2005). Monitoring cytosolic pH of carboxysome-deficient cells of *Synechocystis* sp. PCC 6803 using fluorescence analysis. *Plant Biol (Stuttg)*, 7(4), 342-347. doi:10.1055/s-2005-837710
- Bobik, T. A., Havemann, G. D., Busch, R. J., Williams, D. S., & Aldrich, H. C. (1999). The propanediol utilization (pdu) operon of *Salmonella enterica* serovar Typhimurium LT2 includes genes necessary for formation of polyhedral organelles involved in coenzyme B(12)-dependent 1, 2-propanediol degradation. *J Bacteriol*, 181(19), 5967-5975.
- Borkhsenius, O. N., Mason, C. B., & Moroney, J. V. (1998). The intracellular localization of ribulose-1,5-bisphosphate carboxylase/oxygenase in *Chlamydomonas reinhardtii*. *Plant Physiology*, 116(4), 1585-1591.
- Caspari, O. D., Meyer, M. T., Tolleter, D., Wittkopp, T. M., Cuniffe, N. J., Lawson, T., . . . Griffiths, H. (2017). Pyrenoid loss in *Chlamydomonas reinhardtii* causes limitations in CO₂ supply, but not thylakoid operating efficiency. *J Exp Bot*, 68(14), 3903-3913. doi:10.1093/jxb/erx197
- Castellana, M., Wilson, M. Z., Xu, Y., Joshi, P., Cristea, I. M., Rabinowitz, J. D., . . . Wingreen, N. S. (2014). Enzyme clustering accelerates processing of intermediates through metabolic channeling. *Nat Biotechnol*, 32(10), 1011-1018. doi:10.1038/nbt.3018
- Chang, A., Schomburg, I., Placzek, S., Jeske, L., Ulbrich, M., Xiao, M., . . . Schomburg, D. (2015). BRENDA in 2015: exciting developments in its 25th year of existence. *Nucleic Acids Res*, 43(Database issue), D439-446. doi:10.1093/nar/gku1068
- Chen, P., Andersson, D. I., & Roth, J. R. (1994). The control region of the pdu/cob regulon in *Salmonella typhimurium*. *J Bacteriol*, 176(17), 5474-5482.
- Chiappino-Pepe, A., Tymoshenko, S., Ataman, M., Soldati-Favre, D., & Hatzimanikatis, V. (2017). Bioenergetics-based modeling of *Plasmodium falciparum* metabolism reveals its essential genes, nutritional requirements, and thermodynamic bottlenecks. *PLoS Comput Biol*, 13(3), e1005397. doi:10.1371/journal.pcbi.1005397
- Cox, J., & Mann, M. (2008). MaxQuant enables high peptide identification rates, individualized p.p.b.-range mass accuracies and proteome-wide protein quantification. *Nat Biotechnol*, 26(12), 1367-1372. doi:10.1038/nbt.1511
- Delgado, E., Medrano, H., Keys, A. J., & Parry, M. A. J. (1995). Species Variation in Rubisco Specificity Factor. *Journal of Experimental Botany*, 46(292), 1775-1777. doi:10.1093/jxb/46.11.1775
- Drews, G., & Niklowitz, W. (1956). [Cytology of Cyanophyceae. II. Centroplasm and granular inclusions of *Phormidium uncinatum*]. *Arch Mikrobiol*, 24(2), 147-162.
- Duanmu, D., Wang, Y., & Spalding, M. H. (2009). Thylakoid lumen carbonic anhydrase (CAH3) mutation suppresses air-Dier phenotype of LCIB mutant in *Chlamydomonas reinhardtii*. *Plant Physiol*, 149(2), 929-937. doi:10.1104/pp.108.132456
- Dunford, R. P., Durrant, M. C., Catley, M. A., & Dyer, T. A. (1998). Location of the redox-active cysteines in chloroplast sedoheptulose-1,7-bisphosphatase indicates that its allosteric regulation is similar but not identical to that of fructose-1,6-bisphosphatase. *Photosynthesis Research*, 58(3), 221-230. doi:10.1023/A:1006178826976
- Engel, B. D., Schaffer, M., Kuhn Cuellar, L., Villa, E., Plitzko, J. M., & Baumeister, W. (2015). Native architecture of the *Chlamydomonas* chloroplast revealed by in situ cryo-electron tomography. *Elife*, 4. doi:10.7554/eLife.04889

- Flamholz, A., Noor, E., Bar-Even, A., & Milo, R. (2012). eQuilibrator--the biochemical thermodynamics calculator. *Nucleic Acids Res*, 40(Database issue), D770-775. doi:10.1093/nar/gkr874
- Fujiwara, R., & Itoh, T. (2014). Extensive protein-protein interactions involving UDP-glucuronosyltransferase (UGT) 2B7 in human liver microsomes. *Drug Metab Pharmacokinet*, 29(3), 259-265.
- Genkov, T., Meyer, M., Griffiths, H., & Spreitzer, R. J. (2010). Functional Hybrid Rubisco Enzymes with Plant Small Subunits and Algal Large Subunits ENGINEERED rbcS cDNA FOR EXPRESSION IN CHLAMYDOMONAS. *Journal of Biological Chemistry*, 285(26), 19833-19841. doi:10.1074/jbc.M110.124230
- Gerhardt, R., Stitt, M., & Heldt, H. W. (1987). Subcellular Metabolite Levels in Spinach Leaves : Regulation of Sucrose Synthesis during Diurnal Alterations in Photosynthetic Partitioning. *Plant Physiol*, 83(2), 399-407.
- Gibbs, S. P. (1962). Ultrastructure of Pyrenoids of Algae, Exclusive of Green Algae. *Journal of Ultrastructure Research*, 7(3-4), 247-&. doi:Doi 10.1016/S0022-5320(62)90021-7
- Gibon, Y., Blaesing, O. E., Hannemann, J., Carillo, P., Hohne, M., Hendriks, J. H., . . . Stitt, M. (2004). A Robot-based platform to measure multiple enzyme activities in Arabidopsis using a set of cycling assays: comparison of changes of enzyme activities and transcript levels during diurnal cycles and in prolonged darkness. *Plant Cell*, 16(12), 3304-3325. doi:10.1105/tpc.104.025973
- Giordano, M., Beardall, J., & Raven, J. A. (2005). CO₂ concentrating mechanisms in algae: Mechanisms, environmental modulation, and evolution. In *Annual Review of Plant Biology* (Vol. 56, pp. 99-131). Palo Alto: Annual Reviews.
- Grossman, A. R., Croft, M., Gladyshev, V. N., Merchant, S. S., Posewitz, M. C., Prochnik, S., & Spalding, M. H. (2007). Novel metabolism in Chlamydomonas through the lens of genomics. *Current Opinion in Plant Biology*, 10(2), 190-198. doi:10.1016/j.pbi.2007.01.012
- Holdsworth, R. H. (1971). The isolation and partial characterization of the pyrenoid protein of Eremosphaera viridis. *J Cell Biol*, 51(21), 499-513.
- Hyman, A. A., Weber, C. A., & Juelicher, F. (2014). Liquid-Liquid Phase Separation in Biology. *Annual Review of Cell and Developmental Biology*, Vol 30, 30, 39-58. doi:10.1146/annurev-cellbio-100913-013325
- Jin, S., Sun, J., Wunder, T., Tang, D., Cousins, A. B., Sze, S. K., . . . Gao, Y. G. (2016). Structural insights into the LCIB protein family reveals a new group of beta-carbonic anhydrases. *Proc Natl Acad Sci U S A*, 113(51), 14716-14721. doi:10.1073/pnas.1616294113
- Jungnick, N., Ma, Y., Mukherjee, B., Cronan, J. C., Speed, D. J., Laborde, S. M., . . . Moroney, J. V. (2014). The carbon concentrating mechanism in Chlamydomonas reinhardtii: finding the missing pieces. *Photosynth Res*, 121(2-3), 159-173. doi:10.1007/s11120-014-0004-x
- Kerfeld, C. A., & Melnicki, M. R. (2016). Assembly, function and evolution of cyanobacterial carboxysomes. *Curr Opin Plant Biol*, 31, 66-75. doi:10.1016/j.pbi.2016.03.009
- Kuchitsu, K., Tsuzuki, M., & Miyachi, S. (1988a). Changes of Starch Localization within the Chloroplast Induced by Changes in Co₂ Concentration during Growth of Chlamydomonas-Reinhardtii - Independent Regulation of Pyrenoid Starch and Stroma Starch. *Plant and Cell Physiology*, 29(8), 1269-1278.
- Kuchitsu, K., Tsuzuki, M., & Miyachi, S. (1988b). Characterization of the Pyrenoid Isolated from Unicellular Green-Alga Chlamydomonas-Reinhardtii - Particulate Form of Rubisco Protein. *Protoplasma*, 144(1), 17-24. doi:Doi 10.1007/Bf01320276
- Kuchitsu, K., Tsuzuki, M., & Miyachi, S. (1991). Polypeptide Composition and Enzyme-Activities of the Pyrenoid and Its Regulation by Co₂ Concentration in Unicellular Green-Algae. *Canadian Journal of Botany-Revue Canadienne De Botanique*, 69(5), 1062-1069.

- Mackinder, L. C. M., Chen, C., Leib, R. D., Patena, W., Blum, S. R., Rodman, M., . . . Jonikas, M. C. (2017). A Spatial Interactome Reveals the Protein Organization of the Algal CO₂-Concentrating Mechanism. *Cell*, 171(1), 133-147 e114. doi:10.1016/j.cell.2017.08.044
- Mackinder, L. C. M., Meyer, M. T., Mettler-Altmann, T., Chen, V. K., Mitchell, M. C., Caspari, O., . . . Jonikas, M. C. (2016). A repeat protein links Rubisco to form the eukaryotic carbon-concentrating organelle. *Proc Natl Acad Sci U S A*, 113(21), 5958-5963. doi:10.1073/pnas.1522866113
- Manjunath, S., Lee, C. H., VanWinkle, P., & Bailey-Serres, J. (1998). Molecular and biochemical characterization of cytosolic phosphoglucomutase in maize. Expression during development and in response to oxygen deprivation. *Plant Physiol*, 117(3), 997-1006.
- McKay, R. M. L., & Gibbs, S. P. (1991). Composition and Function of Pyrenoids - Cytochemical and Immunocytochemical Approaches. *Canadian Journal of Botany-Revue Canadienne De Botanique*, 69(5), 1040-1052. doi:DOI 10.1139/b91-134
- McKay, R. M. L., Gibbs, S. P., & Vaughn, K. C. (1991). Rubisco Activase Is Present in the Pyrenoid of Green-Algae. *Protoplasma*, 162(1), 38-45. doi:Doi 10.1007/Bf01403899
- Mettler, T., Muhlhaut, T., Hemme, D., Schottler, M. A., Rupprecht, J., Idoine, A., . . . Stitt, M. (2014). Systems Analysis of the Response of Photosynthesis, Metabolism, and Growth to an Increase in Irradiance in the Photosynthetic Model Organism *Chlamydomonas reinhardtii*. *Plant Cell*, 26(6), 2310-2350. doi:10.1105/tpc.114.124537
- Moore, T. C., & Escalante-Semerena, J. C. (2016). The EutQ and EutP proteins are novel acetate kinases involved in ethanolamine catabolism: physiological implications for the function of the ethanolamine metabolosome in *Salmonella enterica*. *Mol Microbiol*, 99(3), 497-511. doi:10.1111/mmi.13243
- Moroney, J. V., Ma, Y., Frey, W. D., Fusilier, K. A., Pham, T. T., Simms, T. A., . . . Mukherjee, B. (2011). The carbonic anhydrase isoforms of *Chlamydomonas reinhardtii*: intracellular location, expression, and physiological roles. *Photosynth Res*, 109(1-3), 133-149. doi:10.1007/s11120-011-9635-3
- Moroney, J. V., & Ynalvez, R. A. (2007). Proposed carbon dioxide concentrating mechanism in *Chlamydomonas reinhardtii*. *Eukaryotic Cell*, 6(8), 1251-1259. doi:10.1128/Ec.00064-07
- Nagai, T., Ibata, K., Park, E. S., Kubota, M., Mikoshiba, K., & Miyawaki, A. (2002). A variant of yellow fluorescent protein with fast and efficient maturation for cell-biological applications. *Nat Biotechnol*, 20(1), 87-90. doi:10.1038/nbt0102-87
- Ogawa, T., Amichay, D., & Gurevitz, M. (1994). Isolation and characterization of the ccmM gene required by the cyanobacterium *Synechocystis* PCC6803 for inorganic carbon utilization. *Photosynth Res*, 39(2), 183-190. doi:10.1007/BF00029385
- Orth, J. D., Thiele, I., & Palsson, B. O. (2010). What is flux balance analysis? *Nat Biotechnol*, 28(3), 245-248. doi:10.1038/nbt.1614
- Portis, A. R. (1981). Evidence of a Low Stromal Mg Concentration in Intact Chloroplasts in the Dark: I. STUDIES WITH THE IONOPHORE A23187. *Plant Physiol*, 67(5), 985-989.
- Ramazanov, Z., Rawat, M., Henk, M. C., Mason, C. B., Matthews, S. W., & Moroney, J. V. (1994). The Induction of the CO₂-Concentrating Mechanism Is Correlated with the Formation of the Starch Sheath around the Pyrenoid of *Chlamydomonas-Reinhardtii*. *Planta*, 195(2), 210-216.
- Rosenzweig, E. S. F., Xu, B., Cuellar, L. K., Martinez-Sanchez, A., Schaffer, M., Strauss, M., . . . Jonikas, M. C. (2017). The Eukaryotic CO₂-Concentrating Organelle Is Liquid-like and Exhibits Dynamic Reorganization. *Cell*, 171(1), 148-+. doi:10.1016/j.cell.2017.08.008
- Sager, R. (1955). Inheritance in the Green Alga *Chlamydomonas Reinhardtii*. *Genetics*, 40(4), 476-489.
- Saks, V., Beraud, N., & Wallimann, T. (2008). Metabolic compartmentation - a system level property of muscle cells: real problems of diffusion in living cells. *Int J Mol Sci*, 9(5), 751-767. doi:10.3390/ijms9050751

952 Sampson, E. M., & Bobik, T. A. (2008). Microcompartments for B12-dependent 1,2-propanediol
 953 degradation provide protection from DNA and cellular damage by a reactive metabolic
 954 intermediate. *J Bacteriol*, 190(8), 2966-2971. doi:10.1128/JB.01925-07

955 Schellenberger, J., Que, R., Fleming, R. M., Thiele, I., Orth, J. D., Feist, A. M., . . . Palsson, B. O. (2011).
 956 Quantitative prediction of cellular metabolism with constraint-based models: the COBRA
 957 Toolbox v2.0. *Nature Protocols*, 6(9), 1290-1307. doi:10.1038/nprot.2011.308

958 Schindelin, J., Arganda-Carreras, I., Frise, E., Kaynig, V., Longair, M., Pietzsch, T., . . . Cardona, A.
 959 (2012). Fiji: an open-source platform for biological-image analysis. *Nat Methods*, 9(7), 676-
 960 682. doi:10.1038/nmeth.2019

961 Schotz, F., Bathelt, H., Arnold, C. G., & Schimmer, O. (1972). The architecture and organization of the
 962 Chlamydomonas cell. Results of serial-section electron microscopy and a three-dimensional
 963 reconstruction. *Protoplasma*, 75(3), 229-254.

964 Sinetova, M. A., Kupriyanova, E. V., Markelova, A. G., Allakhverdiev, S. I., & Pronina, N. A. (2012).
 965 Identification and functional role of the carbonic anhydrase Cah3 in thylakoid membranes of
 966 pyrenoid of Chlamydomonas reinhardtii. *Biochim Biophys Acta*, 1817(8), 1248-1255.
 967 doi:10.1016/j.bbabi.2012.02.014

968 Spalding, M. H. (2008). Microalgal carbon-dioxide-concentrating mechanisms: Chlamydomonas
 969 inorganic carbon transporters. *Journal of Experimental Botany*, 59(7), 1463-1473.
 970 doi:10.1093/jxb/erm128

971 Sparla, F., Pupillo, P., & Trost, P. (2002). The C-terminal extension of glyceraldehyde-3-phosphate
 972 dehydrogenase subunit B acts as an autoinhibitory domain regulated by thioredoxins and
 973 nicotinamide adenine dinucleotide. *Journal of Biological Chemistry*, 277(47), 44946-44952.
 974 doi:10.1074/jbc.M206873200

975 Stojiljkovic, I., Baumler, A. J., & Heffron, F. (1995). Ethanolamine utilization in Salmonella
 976 typhimurium: nucleotide sequence, protein expression, and mutational analysis of the cchA
 977 cchB eutE eutJ eutG eutH gene cluster. *J Bacteriol*, 177(5), 1357-1366.

978 Sulpice, R., Tschoep, H., M, V. O. N. K., Bussis, D., Usadel, B., Hohne, M., . . . Gibon, Y. (2007).
 979 Description and applications of a rapid and sensitive non-radioactive microplate-based assay
 980 for maximum and initial activity of D-ribulose-1,5-bisphosphate carboxylase/oxygenase.
 981 *Plant Cell Environ*, 30(9), 1163-1175. doi:10.1111/j.1365-3040.2007.01679.x

982 Süß, K. H., Prokhorenko, I., & Adler, K. (1995). In Situ Association of Calvin Cycle Enzymes, Ribulose-
 983 1,5-Bisphosphate Carboxylase/Oxygenase Activase, Ferredoxin-NADP+ Reductase, and
 984 Nitrite Reductase with Thylakoid and Pyrenoid Membranes of Chlamydomonas reinhardtii
 985 Chloroplasts as Revealed by Immunoelectron Microscopy. *Plant Physiol*, 107(4), 1387-1397.

986 Tcherkez, G. G., Farquhar, G. D., & Andrews, T. J. (2006). Despite slow catalysis and confused
 987 substrate specificity, all ribulose bisphosphate carboxylases may be nearly perfectly
 988 optimized. *Proc Natl Acad Sci U S A*, 103(19), 7246-7251. doi:10.1073/pnas.0600605103

989 Teige, M., Melzer, M., & Suss, K. H. (1998). Purification, properties and in situ localization of the
 990 amphibolic enzymes D-ribulose 5-phosphate 3-epimerase and transketolase from spinach
 991 chloroplasts. *European Journal of Biochemistry*, 252(2), 237-244. doi:DOI 10.1046/j.1432-
 992 1327.1998.2520237.x

993 Villarejo, A., Martinez, F., Plumed, M. D., & Ramazanov, Z. (1996). The induction of the CO2
 994 concentrating mechanism in a starch-less mutant of Chlamydomonas reinhardtii. *Physiologia
 995 Plantarum*, 98(4), 798-802. doi:DOI 10.1034/j.1399-3054.1996.980417.x

996 Voit, E. O., Martens, H. A., & Omholt, S. W. (2015). 150 years of the mass action law. *PLoS Comput
 997 Biol*, 11(1), e1004012. doi:10.1371/journal.pcbi.1004012

998 Wang, Y., Duanmu, D., & Spalding, M. H. (2011). Carbon dioxide concentrating mechanism in
 999 Chlamydomonas reinhardtii: inorganic carbon transport and CO2 recapture. *Photosynth Res*,
 1000 109(1-3), 115-122. doi:10.1007/s11120-011-9643-3

- Wang, Y., Stessman, D. J., & Spalding, M. H. (2015). The CO₂ concentrating mechanism and photosynthetic carbon assimilation in limiting CO₂ : how *Chlamydomonas* works against the gradient. *Plant J*, 82(3), 429-448. doi:10.1111/tpj.12829
- Werdan, K., Heldt, H. W., & Milovancev, M. (1975). The role of pH in the regulation of carbon fixation in the chloroplast stroma. Studies on CO₂ fixation in the light and dark. *Biochim Biophys Acta*, 396(2), 276-292.
- Woodger, F. J., Badger, M. R., & Price, G. D. (2005). Sensing of inorganic carbon limitation in *Synechococcus* PCC7942 is correlated with the size of the internal inorganic carbon pool and involves oxygen. *Plant Physiol*, 139(4), 1959-1969. doi:10.1104/pp.105.069146
- Yamano, T., Miura, K., & Fukuzawa, H. (2008). Expression analysis of genes associated with the induction of the carbon-concentrating mechanism in *Chlamydomonas reinhardtii*. *Plant Physiology*, 147(1), 340-354. doi:10.1104/pp.107.114652
- Yamano, T., Tsujikawa, T., Hatano, K., Ozawa, S., Takahashi, Y., & Fukuzawa, H. (2010). Light and Low-CO₂-Dependent LCIB-LCIC Complex Localization in the Chloroplast Supports the Carbon-Concentrating Mechanism in *Chlamydomonas reinhardtii*. *Plant and Cell Physiology*, 51(9), 1453-1468. doi:10.1093/pcp/pcq105
- Yeates, T. O., Crowley, C. S., & Tanaka, S. (2010). Bacterial microcompartment organelles: protein shell structure and evolution. *Annu Rev Biophys*, 39, 185-205. doi:10.1146/annurev.biophys.093008.131418

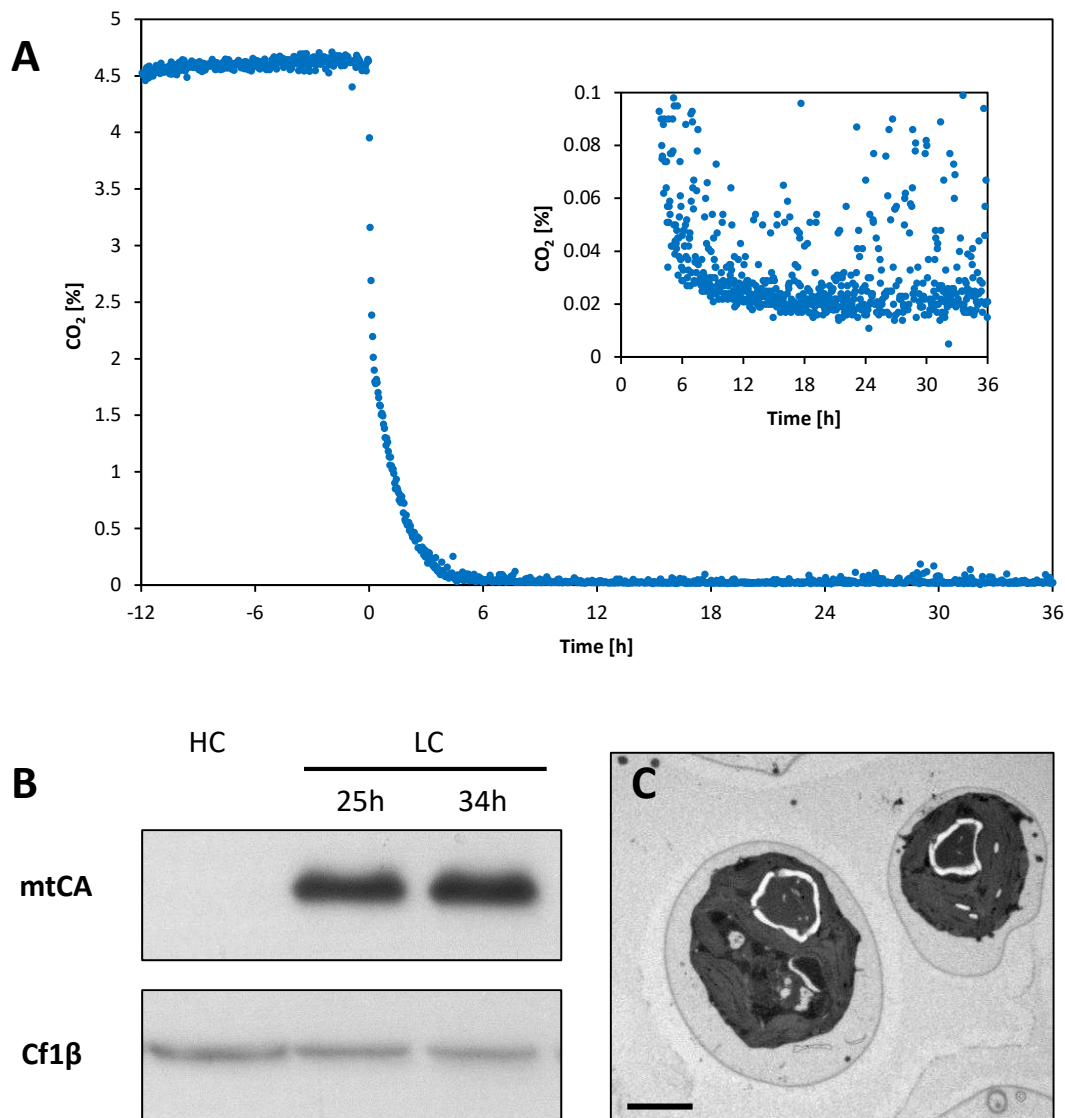


Figure 2-figure supplement 1. Induction of carbon concentrating mechanism (CCM).

Chlamydomonas reinhardtii CC1690 were grown at $46 \mu\text{mol photons} \cdot \text{m}^{-2} \cdot \text{s}^{-1}$, 24°C and bubbled with 5% CO₂ (HC) for two days at constant turbidity in a bioreactor. CO₂ in the outlet air of the bioreactor was measured continuously during a 48 h run (A). From time point zero onwards the culture was aerated with ambient air (0.039% CO₂). The inserted graph shows the same CO₂ data at lower CO₂ concentrations. Cultures were harvested before (HC) and 25 and 34 h (LC) after low-CO₂ exposure for Western blot analysis (B). Protein amounts equivalent to 1 μg chlorophyll were loaded per lane and separated by 12% SDS-PAGE before transferred to a nitrocellulose membrane for detection via chemiluminescence by an antiserum recognizing mtCA (AgriSera Cat# AS11 1737, RRID:AB_10752086). Loading control: CF₁β, β-subunit of the CF₁-component of CF₁F₀-ATP synthase (AgriSera Cat# AS10 1590, RRID:AB_10754669). Transmission electron microscopy (TEM) of cells exposed for 30 h to low CO₂ and 15 min to high CO₂ (LC*; C). Cells were then quenched in the light for metabolite analysis by LC-MS/MS. Measure bar = 2 μm .

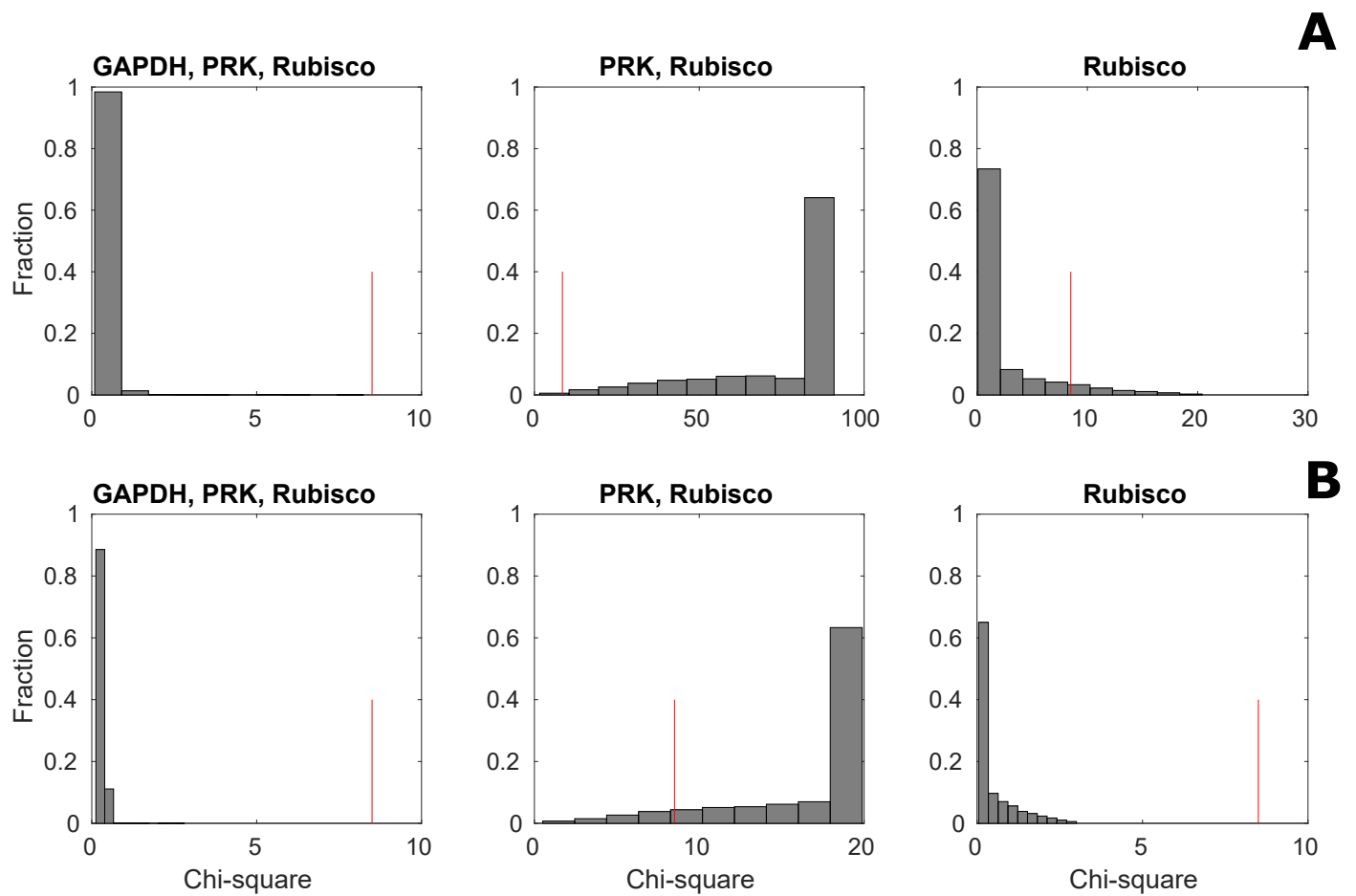


Figure 4-figure supplement 1. Distribution of Chi-square statistic for 5,000 sampled steady-state flux distributions under three different assumptions. Model predictions under non-CCM (HC, A) and CCM-induced (LC*, B) conditions were validated using the Chi-square statistic between predicted and measured total concentration for 11 metabolites over 5,000 sampled steady-state flux distributions. The validation was done under three different assumptions: (i) activity of PRK, Rubisco and GAPDH, (ii) activity of PRK and Rubisco, and (iii) only activity of Rubisco in the pyrenoid. The red line shows the Chi-square statistic corresponding to a significance level of 0.05.

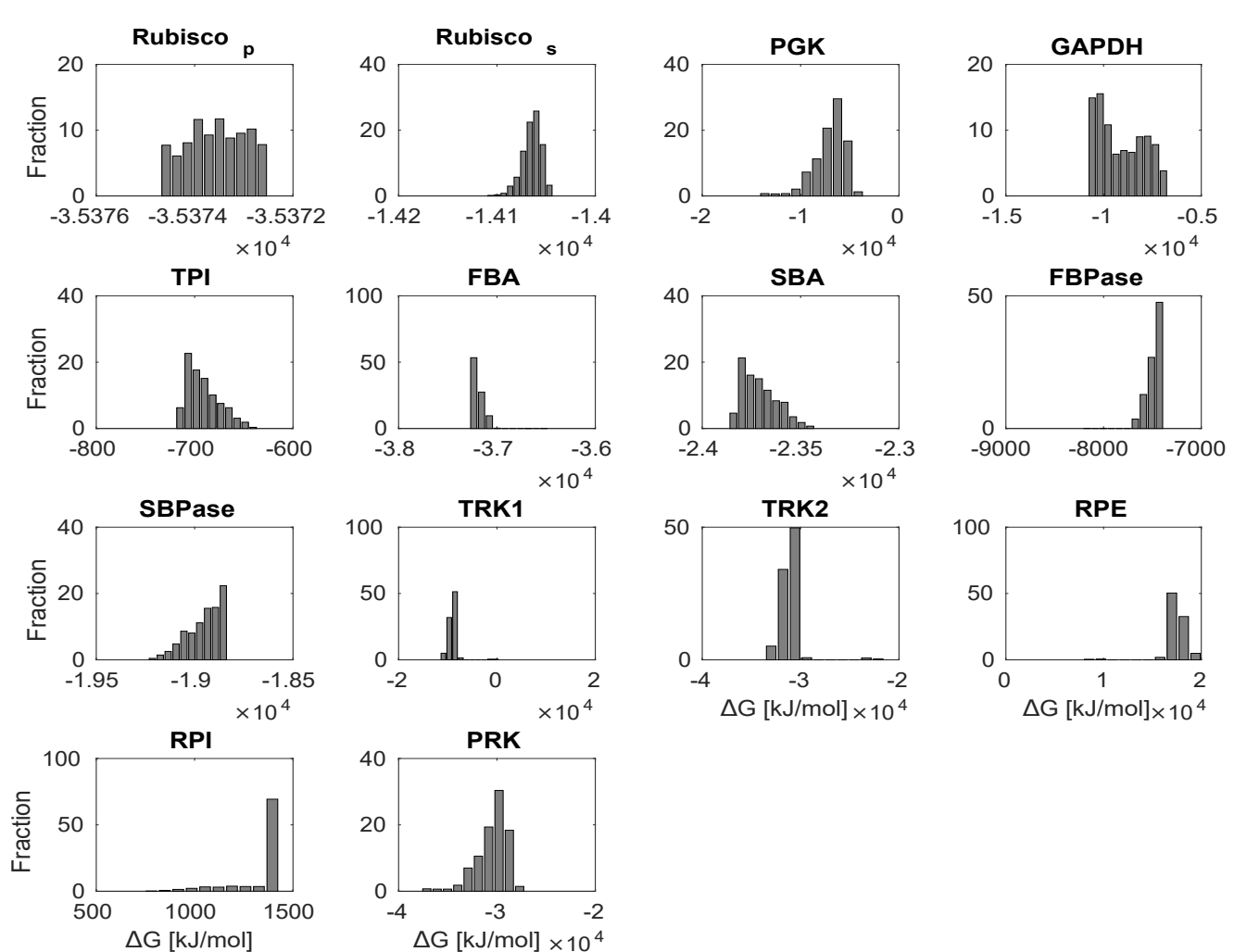
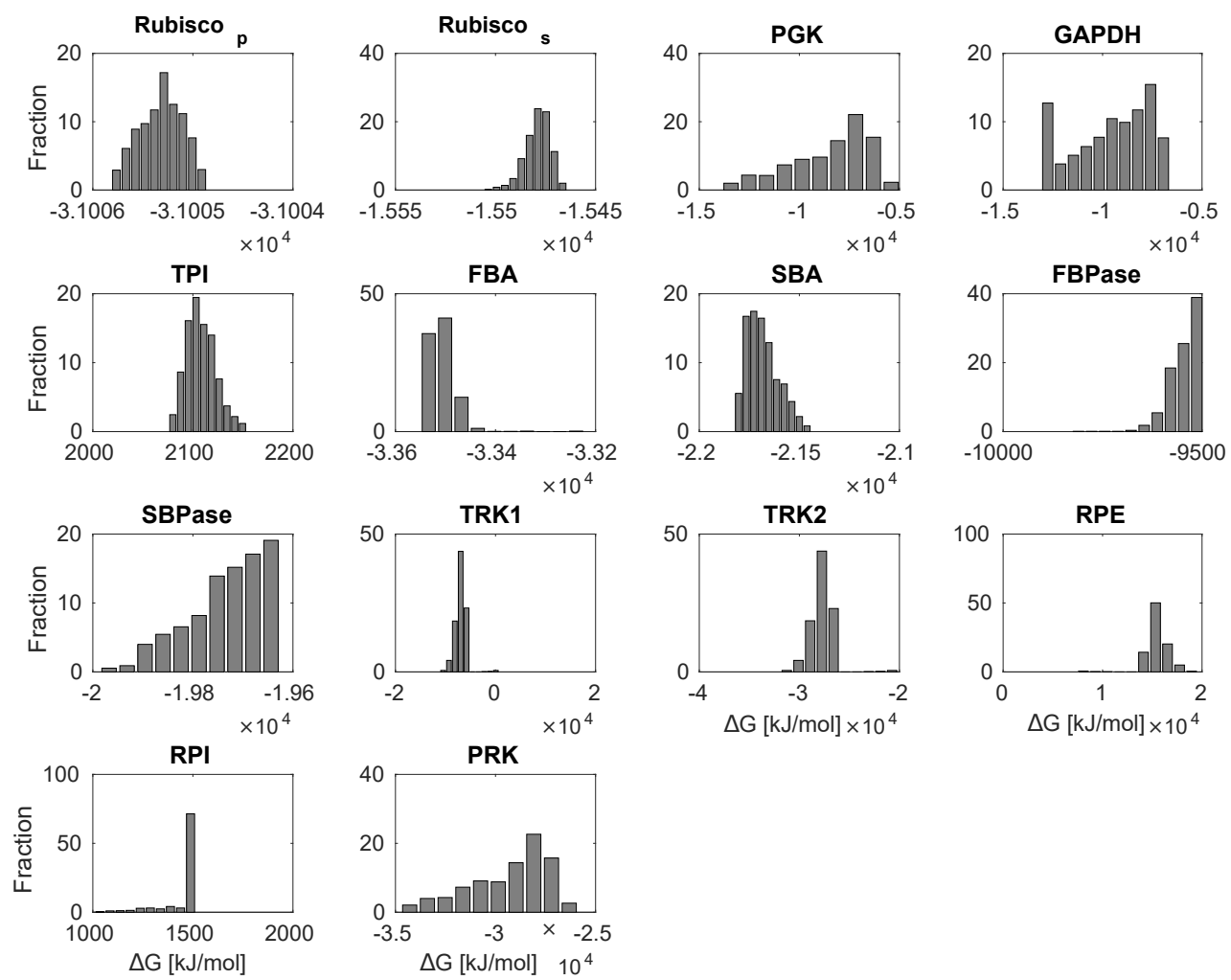


Figure 5-figure supplement 1. Distribution of estimated ΔG values for CBC metabolites over 1,000 sampled steady-state flux distributions under no-CCM (HC; A) and CCM-induced (LC*; B) conditions. The estimated ΔG was negative for all enzymes except RPE and RPI for which $\Delta G > 0$. In addition, TRK was found to be the only enzyme operating in both directions.

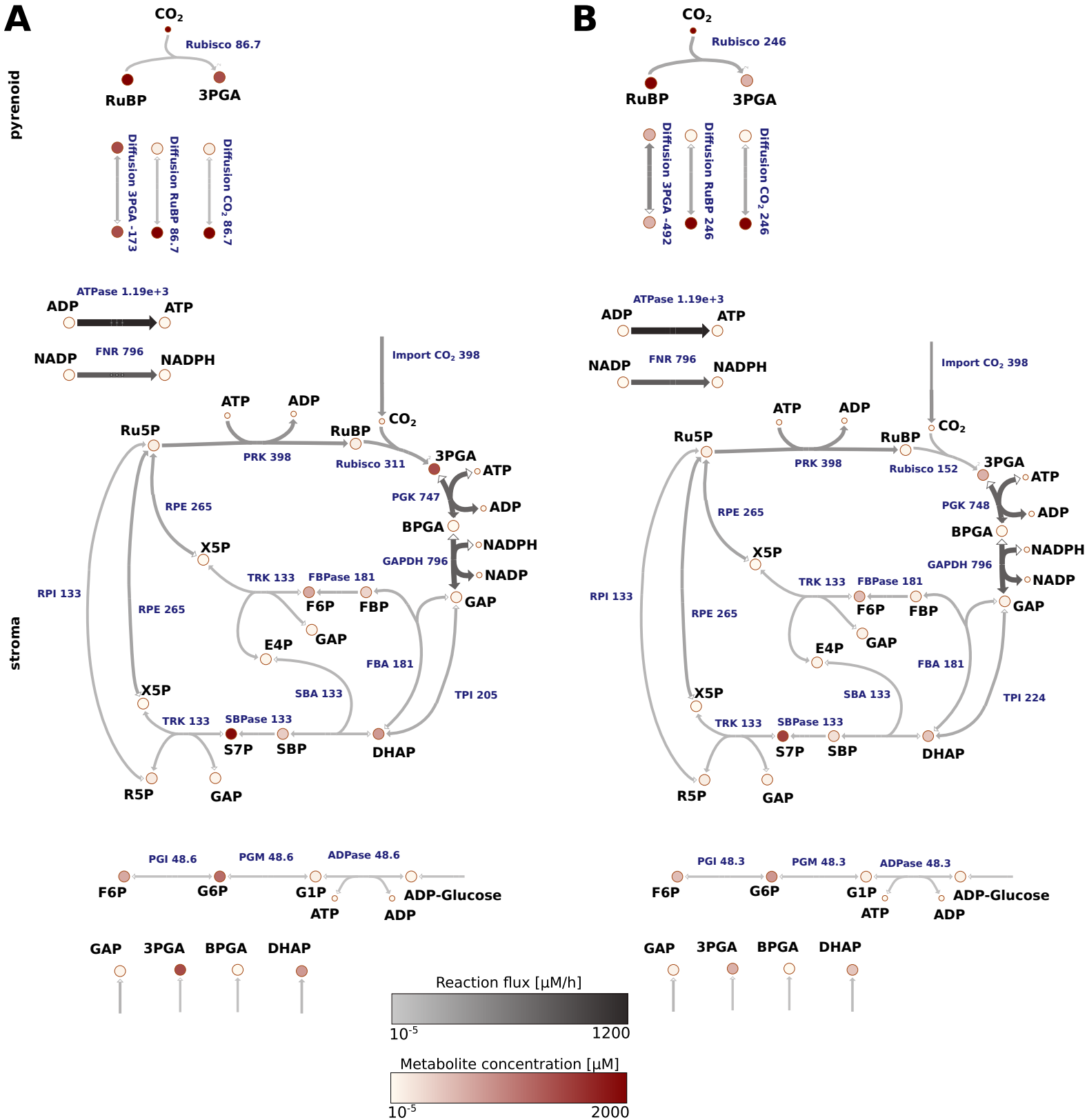


Figure 6-figure supplement 1. Reaction flux estimated for *Chlamydomonas reinhardtii* cells grown under non-CCM (HC; A) and CCM-induced (LC*; B) conditions. The average values of the flux and total metabolite concentration are indicated by a colour code (see legend) and size of the arrows (denoting the reactions). The actual values are provided in Supplementary files 5 and 6. The main difference observed between HC and LC* conditions was an increased flux through Rubisco in the pyrenoid under LC* and an increase in the flux of RuBP and 3PGA into the pyrenoid and from the pyrenoid, respectively, under LC*. The flux through the Calvin-Benson cycle located in the stroma, however, was similar under both conditions.